ISPRS Journal of Photogrammetry and Remote Sensing 187 (2022) 240–258

Contents lists available at ScienceDirect

ISPRS Journal of Photogrammetry and Remote Sensing

journal homepage: www.elsevier.com/locate/isprsjprs

A new East African satellite data validation station: Performance of the LSA-SAF all-weather land surface temperature product over a savannah biome

T.P.F. Dowling [a], M.F. Langsdale [a,b,*], S.L. Ermida [c,d], M.J. Wooster [a,b], L. Merbold [e,1], S. Leitner [e], I.F. Trigo [c,d], I. Gluecks [e,h], B. Main [a], F. O'Shea [a], S. Hook [f], G. Rivera [f], M.C. De Jong [a], H. Nguyen [a], K. Hyll [g]

[a] Department of Geography, King's College London, Bush House (NE), 40 Aldwych, London WC2B 4BG, United Kingdom
[b] NERC National Centre for Earth Observation (NCEO), UK
[c] Instituto Português do Mar e da Atmosfera (IPMA), Lisbon, Portugal
[d] Instituto Dom Luiz (IDL), Faculdade de Ciências, Universidade de Lisboa, Lisbon, Portugal
[e] Mazingira Centre, International Livestock Research Institute (ILRI), PO Box 30709, Nairobi, Kenya
[f] Jet Propulsion Laboratory, California Institute of Technology, Pasadena, CA 91109, USA
[g] Skogforsk, the Forestry Research Institute of Sweden, Uppsala, Sweden
[h] ILRI Kapiti Wildlife Conservancy, ILRI Kapiti Research, PO Box 30709, Nairobi, Kenya

ARTICLE INFO

Keywords:
Land surface temperature
Meteosat
Validation
Savannah
All-sky
Thermal

ABSTRACT

We describe a new satellite data validation facility located in a savannah biome at the International Livestock Research Institute (ILRI) Kapiti Research Station (Kenya). The facility is focused on satellite land surface temperature (LST) and is equipped with multiple ground-viewing infrared radiometers across four sites. The in-situ LST observations are upscaled to match satellite LST products using a geometric illumination model. The in-situ sensor network represents a step-forward in LST validation in East Africa and savannah biomes. To our knowledge this is the first time that such an extensive network of LST radiometers and supporting measurements has been installed in sub-Saharan Africa, or a savannah. With this network we capture surface heterogeneity in a manner that has not previously been possible. The LST ground data from this station collected between October 2018 and March 2019 is used to evaluate the new Land Surface Analysis Satellite Application Facility (LSA-SAF) all-sky LST product (MLST-AS) that blends clear-sky infrared-retrieved LSTs with LSTs derived from a land surface energy balance model to fill gaps due to cloudy conditions. Comparison against the in-situ LSTs indicates overall accuracy, precision, and root-mean-square error (RMSE) of MLST-AS to be 2.02 K, 1.38 K and 3.64 K respectively. The infrared-retrieved LST component of MLST-AS under clear skies has an accuracy, precision and RMSE of 1.16 K, 0.8 K and 3.16 K respectively. The energy balance model-based component of MLST-AS has performance statistics of 3.02 K, 1.38 K and 4.16 K. The MLST-AS energy balance model component is observed to perform worse when surface moisture is present, underestimating night-time and daily maximum temperatures by between 2 and 4 K in the 24 h following surface water deposition as precipitation or dew.

1. Introduction

Land surface temperature (LST) is a key parameter of the land surface that determines energy exchanges at the land–atmosphere boundary. It is an essential variable for calculating surface fluxes and turbulence and consequently has multiple applications in areas including meteorology, climatology, and agricultural studies (Good et al., 2017; Vancutsem et al., 2010; Marques da Silva et al., 2015). LST is commonly derived from infrared observations made by several space-borne imaging radiometers, for example from the polar-orbiting Moderate Resolution Imaging Spectroradiometer (MODIS) onboard the Terra and Aqua satellite platforms. However, by using data from geostationary sensors such as

* Corresponding author at: Department for Geography, King's College London, Bush House NE Wing, 40 Aldwych, London, WC2B 4BG, UK
E-mail address: mary.langsdale@kcl.ac.uk (M.F. Langsdale).
[1] Now at Agroscope, Department Agroecology and Environment, Reckenholzstrasse 191, 8046, Zurich, Switzerland.

https://doi.org/10.1016/j.isprsjprs.2022.03.003
Received 1 October 2021; Received in revised form 9 February 2022; Accepted 4 March 2022
Available online 21 March 2022

the Spinning Enhanced Visible and Infrared Imager (SEVIRI) onboard Meteosat Second Generation (MSG), a higher temporal resolution of LST retrieval can be achieved that covers the full diurnal cycle. This is a significant advantage for applications that require an accurate estimate of LST diurnal flux such as vegetation and agricultural applications (e.g., Anderson and Kustas, 2008, Chen et al., 2017).

EUMETSAT's Satellite Application Facility on Land Surface Analysis (LSA-SAF) have developed a long-standing Longwave Infrared (LWIR) LST algorithm applied to geostationary LWIR SEVIRI observations based on the generalised split-window (GSW) approach initially developed for the Advanced Very-High-Resolution Radiometer (AVHRR) and MODIS (Wan & Dozier, 1996). The reader is directed to Martins et al. (2018) for the implementation and calibration of the GSW as used in the SEVIRI product. Errors in the LST retrievals made via the GSW method depend on uncertainties in: (i) the surface emissivity assumed, (ii) the water vapour content of the atmosphere, and (iii) the satellite view angle (Trigo et al., 2008; Trigo et al, 2021).

Specification of surface emissivity is a particular issue over structured heterogeneous landscapes such as the savannah biome because the anisotropy and variability of emissivity among pixels within these land cover types is not well captured in the emissivity maps used during LST retrieval (Sobrino et al., 2001). Furthermore, dry-season barren soils and sparse vegetation are characterized by relatively low emissivities and high uncertainties while wet-season vegetation are characterized by higher emissivities. Errors in surface emissivity estimation over savannah biomes are particularly acute when a strongly dichotic wet-dry season triggers rapid green up and therefore changes in emissivity that may not be immediately reflected in an assigned emissivity value (Guillevic et al., 2013; Chehbouni et al., 2001; Liu et al., 2020). In general, emissivity errors are also higher under dry atmospheric conditions, further contributing to IR retrievals being particularly challenging over semi-arid and arid regions (Kim and Hogue, 2013). The LST errors that arise from these effects are a critical flaw that can limit the uptake of satellite LST data into both climate models (Reichle et al., 2010) and agricultural monitoring (Jarvis et al., 2003). Consequently, there is a pressing need to establish the performance of LST retrievals in seasonally vegetated areas through validation stations that can capture the heterogeneity of said environments, whilst also providing sufficient contextual environmental data to allow for the identification of sources of error.

However, Sub-Saharan Africa and the savannah biome that makes up almost half of the continent's land cover (~8 million km) have no active ground-based (in-situ) stations for the validation of satellite LST products. Furthermore, most previous validation studies on the continent have focused on homogeneous desert and bare soil sites (Wan 2014, Göttsche et al., 2016). To our knowledge, there has only been one site on the African continent, located in Dahra (Senegal, West Africa), that was able to examine clear-sky LSTs in the context of savannah type vegetation (in this case, a tiger-bush biome) (Göttsche et al., 2016). Data from this station was used to validate the SEVIRI GSW-derived clear-sky LST product and identified that when data from the rainy season was removed, the highest mean root-mean-square error (RMSE) for SEVIRI LWIR observations was 1.6 K, with a mean absolute bias of 0.1 K. However, when data from the rainy season was included, the RMSE was found to vary between −0.11 K and 7 K (Göttsche et al., 2016). This latter statistic is a significant margin of uncertainty, suggesting that the SEVIRI LST product does not sufficiently capture the strong seasonality of vegetation in response to wet-dry seasons. However, there were multiple data gaps in this study due to technical problems, theft, and cloud. Furthermore, their study relied upon a single mast in a pixel. While this is suitable for homogeneous regions such as deserts, it is not suitable for savannah environments where there is greater spatial variability of LSTs and increased surface anisotropy (Guillevic et al., 2012; Ermida et al., 2014). The lack of validation sites in savannah biomes and these findings from Göttsche et al. (2016) support the need for further investigation into the accuracy and precision of LST retrieval over such environments.

The need for further testing of satellite LST products in the savannah environment is further supported by the work of Rasmussen et al. (2011) who used the afore-mentioned Dahra site of Göttsche et al. (2016) to investigate the impact of structured canopies on clear-sky SEVIRI LST accuracy. They found that the impact of tree canopy directional effects on LST accuracy was up to 2 K during the day and, most importantly, that diurnal timing and amplitude of the effect changes throughout the year. This is a clear signal that both the presence of isolated stands of trees and the existence of a wet-dry season are confounding factors in satellite LST determination over savannahs. Neither of these factors are currently considered in the operationally available LST products of SEVIRI, nor those of polar orbiters such as MODIS (Hulley et al., 2012) and Sentinel 3′s Sea and Land Surface Temperature Radiometer (SLSTR) (Remedios, 2012). Nor are such elements typically considered in the ground validation schema of said operational products (e.g., Hulley et al., 2021; Trigo et al, 2021). The preference instead is to use large-scale, homogenous, validation targets due to the difficulty of obtaining representative measurements at the scale of the satellite pixel, with multiple instruments of the same instrument type required to characterize each component of the landscape in heterogeneous environments (Duan et al., 2019; Guillevic et al., 2012).

Satellite-retrieved LSTs over tropical latitudes are further impacted by increased cloud cover over these regions. As clouds block the LWIR radiance emitted from the Earth's surface from reaching the spaceborne sensor, the GSW approach to LST retrieval only works for clear sky pixels. If LWIR GSW observations are relied upon alone, there can therefore be large data gaps (Kerr et al., 1992). Such data gaps are a significant problem for downstream applications of LST (Li et al., 2018). To overcome this limitation, there have been many recent attempts to provide 'all-weather' LST products that fill any gaps due to cloud cover (e.g., Dash et al., 2002; Prigent et al., 2016; Duan et al., 2017). A common approach has been to use passive microwave (PM) radiation measurements that penetrate cloud cover (McFarland et al., 1990). However, PM radiometers exist only on polar-orbiting satellites, so coverage of the full LST diurnal cycle is not possible. Furthermore, the measurements are spatially coarse (more than 10 km) as compared to thermal sensors (30 m to 5 km). By contrast, MSG SEVIRI offers LWIR measurements at a spatial resolution of 3 km at nadir every 15 min. In addition to these differences, the penetration depth of PM radiation into the land surface is different to the skin temperatures obtained when using LWIR sensors which can lead to difficulties when blending the two types of products (Song et al., 2019).

A suitable alternative approach to fill cloud gaps in LWIR-derived satellite LST products at an appropriate spatial and temporal resolution is using an energy balance model that enables calculation of the surface skin temperature (e.g., Fu et al., 2019). LSA-SAF run an energy balance model as part of their evapotranspiration product delivery chain (Ghilain et al., 2011). The model is based on the physics of the Tiled European Centre for Medium-Range Weather Forecasts (ECMWF) Surface Scheme for Exchange Processes over Land (TESSEL; van den Hurk et al., 2000; Viterbo & Beljaars, 1995) and on H-TESSEL (Albergel et al., 2012; Balsamo et al., 2009). The model runs every 30 minutes and uses the downwelling and upwelling surface radiative fluxes and surface albedo as inputs, as well as vegetation parameters, soil moisture information and a snow mask (Martins et al., 2018). The new LSA-SAF Meteosat Land Surface Temperature – All Sky (MLST-AS) product blends the skin temperatures coming from this energy balance model with LST data coming from the existing clear-sky SEVIRI LST product to fill cloud obscured pixels (Martins et al., 2018). In this way the product benefits from the advantages offered by the LWIR estimated LSTs at clear-sky pixels – which are independent of any model representation and remain driven by physical observations – whilst also providing complete data cover of the SEVIRI full disk image by filling cloudy pixels with skin temperatures derived from the energy balance model. The all-weather LST product is produced at the native SEVIRI pixel scale (~3 km

spatial sampling at nadir) every 30 minutes (Martins et al., 2018).

Initial validation attempts of both the energy balance model and MLST-AS are promising although limited. Considering first the energy balance model validation, work on modelled skin temperatures (Trigo et al., 2015; Orth et al., 2017) has shown that the type of energy balance model used to generate the MLST-AS product tends to misrepresent the amplitude of the diurnal cycle of LST over arid and semi-arid regions. In addition, preliminary work by Ghilain (2018) demonstrated that in cases of no soil moisture availability and high incoming solar radiation, the uncertainty of the modelled outputs is increased. These findings indicate that any evaluation of the MLST-AS product should evaluate the LWIR and modelled portions of the MLST-AS product separately in order to identify if this is an issue over the savannah environment.

The only validation studies of MLST-AS yet have been carried out by Martins et al. (2019) and Martins & Dutra (2020). Martins et al. (2019) tested against three LST ground observation stations – Evora (Mediterranean, Portugal), Kalahari (Desert, Southern Africa) and Gobabeb (Steppe, Namibia) – for 10 days in January 2010 and 10 days in July 2010. Component temperature measurements made in Evora were upscaled using the geometric upscaling model of Ermida et al. (2016) to account for heterogeneity at the pixel scale. No upscaling was carried out for the other two sites due to their relative homogeneity. Overall, the mean accuracy for the MLST-AS product was 0.1 K, with a precision of 1.2 K and a root-mean squared difference (RMSD) of 2.7 K. The RMSDs for Evora, Kalahari and Gobabeb were 2.81, 3.09 and 2.23 K respectively. Martins & Dutra (2020) compared data from MLST-AS against data from 33 in-situ stations between February and December 2018 and found an overall accuracy of 0.0 K and an RMSE of 2.9 K for MLST-AS. However, the authors of this study observed a distinct difference in the performance over more homogeneous surfaces (bare soil, crop and grassland) and the performance over any forested regions, with significantly decreased performance for the latter. These statistics are encouraging but given that the sites considered were either 'simple' in their composition or were subject to increased errors attributed to heterogeneity and all sites considered are not equivalent to the savannah landscape that had proven troublesome in the work of Göttsche et al. (2016), there is also a clear need for further validation of MLST-AS.

In this paper, the establishment of a comprehensive LST validation site in the African savannah biome is first detailed. The site has multiple tower mounted LWIR radiometers on different masts within one SEVIRI pixel which are measuring different components of the landcover separately. The establishment of the site and the derivation of the ground truth in-situ LSTs using the data from the tower-based radiometers follow the protocols set out in Guillevic et al. (2018), Göttsche et al. (2016) and GBOV (2018). The LWIR radiometers are supported by a full eddy-covariance and meteorology installation that provides vital contextual environmental information. The in-situ LST data from these radiometers are up-scaled to the scale of the SEVIRI pixel using the geometric illumination model of Ermida et al. (2014). Data from the site collected between October 2018 and March 2019 is then used in the first independent validation of the all-weather product MLST-AS.

This work represents a significant step forward for in-situ and satellite LST retrieval over savannah type vegetation regions, the primary advantage of the site being the use of multiple radiometers on multiple masts which allows for a better representation of the satellite scale LST by the ground measurements. To our knowledge this is also the first time that such an extensive network of LST radiometers and supporting measurements has been installed in sub-Saharan Africa or a savannah, and the first time such an extensive network of in-situ LST instrumentation has been used to upscale a heterogeneous target in a LST validation study.

2. Site description

The validation site is based at the Kapiti Research Station (owned and managed by the International Livestock Research Institute, ILRI) in Kenya. Figs. 1 and 2 illustrate the location of the site within ILRI Kapiti Wildlife Conservancy (-1.6083°, 37.1327°). Kapiti is situated 1650 m above sea level and experiences two rainy seasons annually, typically between March – May and October - December. The area is flat and homogenous in its assemblage of grassland with sparse tree and shrub cover. The LWIR radiometers are mounted on masts to observe the grass canopies, which are a mixture of dense grasses between 30 and 70 cm in height, and grazed grass-soil complexes where the canopy is typically 5–30 cm in height. Four masts are spread over the northern area of Kapiti Ranch Wildlife Conservancy, with the sensor packages for each mast set out in Table 1. The eddy-covariance system is co-located with Mast 1. Masts 2, 3, and 4 are in flat areas which have less than 10% tree cover across the surrounding 5–10 km^2. The tree canopy under observation by the infrared radiometer at Mast 3 is that of a mature Acacia. This tree species has small finely divided leaflets and long thorns in a dense crown canopy structure. At Mast 4 the surface has been overgrazed and there is little vertical canopy structure other than scattered and isolated clumps of invasive herbaceous species. During the dry season the grass canopies are completely senesced. Between the four masts we sample all three levels of grazing across the ranch; moderately grazed (Masts 1 and 2), lightly grazed (Mast 3) and over-grazed (Mast 4).

Sensors were mounted 1 m from the top of the mast with the masts set to a height of 14.5 m. Instrumentation varied between the masts, with the minimum sensor package for each mast consisting of a vegetation monitoring camera (Canon 500D DSLR RGB), a surface-looking Heitronics KT15.85 IIP precision radiometer (9.6–11.5 μm) (Göttsche et al., 2016) and a surface-looking quasi-nulling Series 500 radiometer manufactured by NASA's Jet Propulsion Laboratory (NASA-JPL) (8 – 14 μm) (Hook et al., 2005; Hook et al., 2007; Donlon et al., 2014). Each LST mast was powered by one 12 V solar panel, feeding a 12 V marine-leisure battery housed in a fan-cooled fibreglass box along with the solar charge controller. The DSLR vegetation monitoring cameras were powered directly from the battery through a custom voltage regulator. Power was supplied and regulated to the radiometers by a Campbell CR300 logger, equipped with a 100 Ω resistor. The logger and all connections are located within a Campbell ENC14/16 enclosure for insulation and protection. Each NASA-JPL radiometer operates with an 18° half-angle field of view (FoV) and is calibrated by the manufacturer to an accuracy of ±0.1 °C (Abrams et al., 1999). The commercial Heitronics KT15.85 IIP has reported absolute accuracy in the field of ±0.5 K plus 0.7% of the temperature difference between target and housing temperature. The FoV of the Heitronics radiometer is non-linear and thus FoV footprint is provided by the manufacturer via a proprietary tool. At each LST mast, the Heitronics radiometers look north whilst JPL radiometers look east. The co-mounted DSLR cameras allow for concordant monitoring of vegetation and canopy state whilst also allowing for the reconstruction of conditions in the event of an unknown sensor error. Fig. 3 summarises the observation angle, mounting height, sensor lens view angle and subsequent ground FoV of the two different types of LWIR radiometer.

Due to non-unity emissivity of the surface, the downward pointing LWIR radiometric measurements contain a component of reflected downwelling LWIR radiance, which must be estimated in order to retrieve accurate LSTs from the radiometric measurements. Therefore, an additional Heitronics radiometer was installed on Mast 3 to observe the sky at 53° zenith angle, facing away from the sun, to measure the sky brightness temperature as a proxy for downwelling radiation (Kondratyev, 1969; García-Santos et al., 2013).

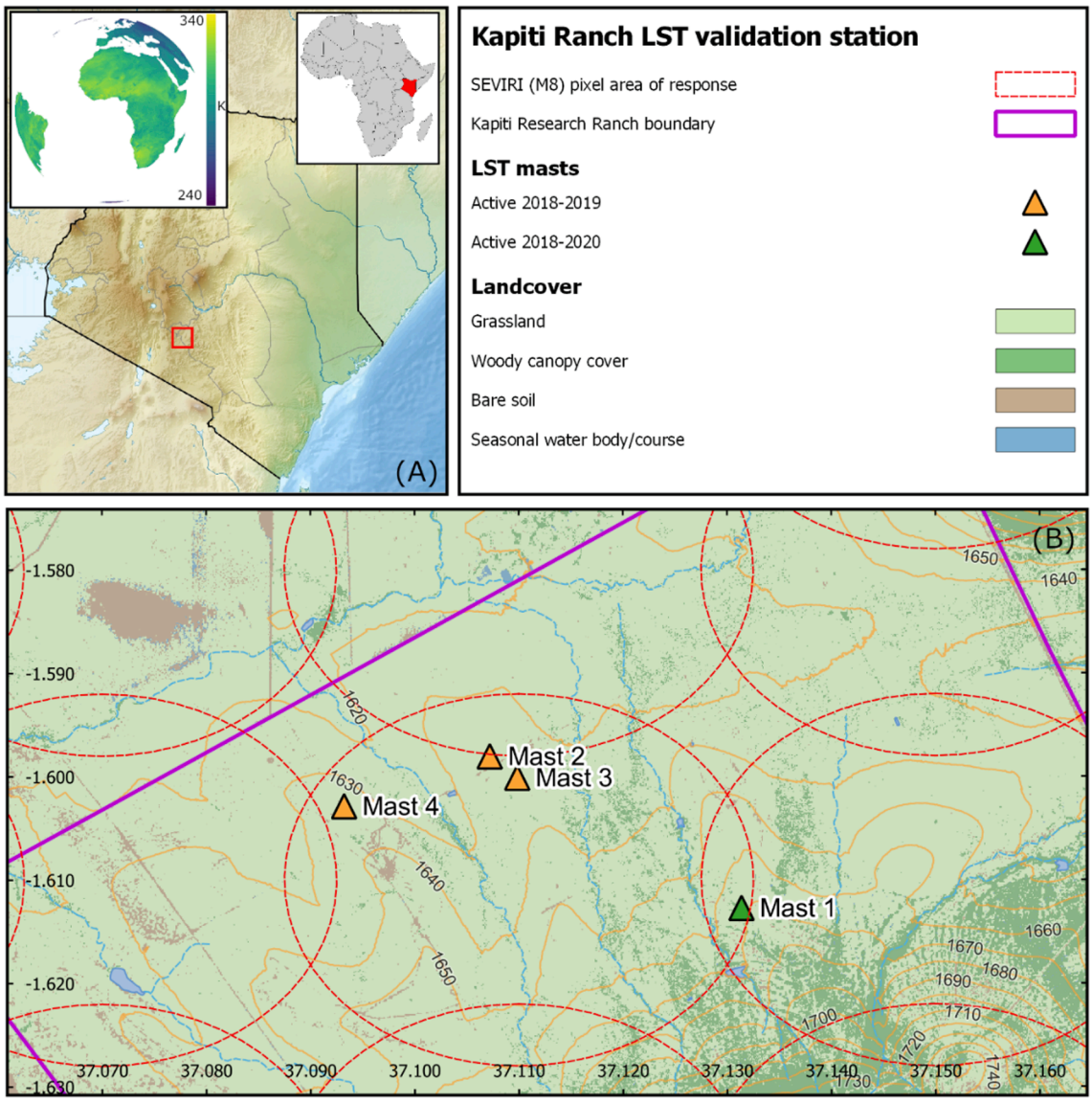

Fig. 1. Location of Kapiti Research Ranch and the sensor masts across ILRI Kapiti Wildlife conservancy. Panel (A): Overview of the location of the Kapiti in the context of Kenya, including inset top left; SEVIRI MSG full disk all-weather LST example data (in Kelvin). Panel (B): Map of the northern half of ILRI Kapiti Wildlife conservancy, with LST measurement sites for both configurations and MSG SEVIRI approximate pixel response area. Landcover classification generated from Sentinel 2 using manually generated training data and a Random Forest based classification (Gislason et al., 2006).

Prior to deployment in the field all radiometers were calibrated using a NIST-traceable blackbody (Omega BB701) in an environmentally controlled chamber. The calibration relationships derived from this procedure were applied to all the in-situ radiometer measurements. Further detail on the calibration procedure and results is available in the supplementary material (see S-1).

3. Data and methods

The Python scripts used to implement the methods detailed below are available at: https://github.com/tpfd/LandSurfaceTemperature-at-Kapiti. The ground validation data and associated metadata as used in this paper are available from: https://doi.org/10.18742/17197814.v1.

3.1. Satellite data

The satellite product considered for validation is the LSA-SAF MLST-AS product described in Section 1. This dataset is available from: https://landsaf.ipma.pt/en/products/land-surface-temperature/mlstas/. We validate the full range of MLST-AS data between October 2018 and March 2019, with one full disk of LST observations available every 30 min (see left-hand insert of Fig. 1, panel A for an example of the full disk). The ground resolution of each pixel varies non-linearly with latitude-longitude (Schmetz et al., 2002). Over the Kapiti site the area of response for each pixel is approximately 4.5 km in the x-axis and 4 km in the y-axis (Fig. 1, main panel B). A key motivation for the choice of a geostationary platform against which to validate with this new ground station is the high frequency of data available as compared to a polar orbiting satellite. By using a geostationary platform, we can validate against many thousands of observations of the same pixel rather than the

Fig. 2. Overview of ground conditions and typical SEVIRI pixel composition at Kapiti. (A) Partially grazed grass canopy during the rainy season, viewed from a vegetation monitoring camera on Mast 1. (B) Heavily grazed grass canopy with significant invasive species penetration in the dry season viewed from Mast 2. (C) Acacia tree canopy at the start of the dry season viewed from Mast 3. (D) Over-grazed soil-grass complex a month intro the dry season at Mast 4. (E) Dense senesced grass canopy at Mast 3 observed from the ground at the height of the dry season. (F) General view of Mast 3 after a week of rains.

few hundred that a polar orbiter such as MODIS would provide over the same time period.

3.2. In-situ LST determination

As per Guillevic et al., (2018), in-situ LST can be derived from the radiance-equivalent of the LWIR radiometer brightness temperatures (BT) (eq. (1)):.

$$LST_{ground} = B_{\lambda}^{-1}\left[\frac{1}{\varepsilon_{\lambda}}\left(L_{ground,\lambda} - (1-\varepsilon_{\lambda})L_{sky,\lambda}\downarrow\right)\right] \quad (1)$$

where ε_{λ} is the surface spectral emissivity at wavelength λ, or representative of the surface emissivity within the given spectral window that is centred on λ. $B_{\lambda}^{-1}(L)$ is the inverse Planck function describing the BT equivalent to the black body radiance (L), $L_{ground,\lambda}$ is the observed ground surface radiance and $L_{sky,\lambda}\downarrow$ is the downwelling radiance measured by the sky-viewing radiometer.

The retrieval of each of these parameters and uncertainty derivation is detailed in Sections 3.2.1–3.2.4., with upscaling to satellite equivalent LSTs in Section 3.2.5.

3.2.1. Radiometer brightness temperature to radiance

The ground-based radiometers output BT values based on voltage measurements, via the calibration equation supplied by the manufacturer. These BT are processed to blackbody equivalent spectral radiances using the Planck function at the effective central wavelength (2):

$$L(\lambda, T) = \frac{C_1}{\lambda^5\left(e^{\frac{C_2}{\lambda T}} - 1\right)} \quad (2)$$

Table 1
Sensor package summary of the Kapiti LST monitoring site. NASA-JPL = quasi-nulling infrared radiometer, the measurement sequence is made every 5 minutes and takes 1 minute to complete. Heitronics (ground) = infrared radiation pyrometer, model KT15.85-IIP. Measurement made every 5 minutes. Heitronics (sky) = measurement every 5 minutes. Field of views, look directions and view angles are presented in Fig. 3.

Site	Radiometers	Cameras	Other sensors	Lat-Lon
1	NASA-JPL Heitronics (ground)	Vegetation RGB	Eddy-covariance system and full meteorological station	−1.6029 37.0932
2	NASA-JPL Heitronics (ground)	Vegetation RGB	–	−1.5980 37.1072
3	NASA-JPL Heitronics (ground) Heitronics (sky)	Vegetation RGB Sky RGB	–	−1.6001 37.1098
4	NASA-JPL Heitronics (ground)	Vegetation RGB Vegetation NIR	–	−1.6127 37.1314

where $L(\lambda, T)$ is the spectral radiance, $C_1 = 2hc^2$, $C_2 = \frac{hc}{k}$, λ = radiometer central wavelength (μm) and T = BT (K). The constants are: h = Planck constant ($6.6260693 \times 10^{-34} Js$), c = speed of light ($2.99792458 \times 10^{8} ms^{-1}$) and k = Stefan-Boltzman constant ($1.380658 \times 10^{-23} W/m^{-2}K^{-4}$).

Given the approximately symmetric spectral response function of the Heitronics KT15.85 radiometer (see S-3 in the supplementary material), previous work has assumed a static central wavelength (λ) of 10.55 μm for Heitronics radiometers when calculating blackbody equivalent spectral radiances from BT observations (Göttsche et al., 2016). However, the potential errors from this assumption become larger when using radiometers with wider spectral windows, such as the NASA-JPL. This is especially true when using both a sky-pointing radiometer to retrieve downwelling radiance and a ground pointing radiometer, due to the varying relative response of the Planck function for clear sky and heated sub-tropical ground surface observations – two very different temperatures. We therefore calculate the effective central wavelength for each paired observation of the ground and sky. The method used to do this and the impact on observed LST is detailed in S-3 in the supplementary material.

3.2.2. Emissivity

The emissivity of a target is the effectiveness of the target in emitting energy as thermal radiation. Estimation of the surface emissivity of an observed target is essential to deriving the correct surface temperature from the detected infrared brightness temperature or spectral radiance. However, it is difficult and unreliable to measure vegetation emissivity in the field (Langsdale et al., 2020) and there are many problems inherent in returning vegetation samples over long distances to suitable laboratory facilities (Rubio et al., 2003). Therefore, we take surface emissivity values generated concurrently with the satellite LST values from the LSA-SAF LST product. The LSA-SAF emissivity product (Trigo et al., 2008) uses a fractional vegetation cover (FVC) based method to calculate the per-pixel emissivity contributions from the vegetation and bare soil components. The land cover classes used are those from the International Geosphere–Biosphere Program database (Loveland et al., 2000). The emissivity values used in the fraction calculation are from laboratory measurements of a variety of surface types and cover, primarily sourced from the John Hopkins University Library (Meerdink et al., 2019a, 2019b). A benefit of using the satellite FVC based method to drive in-situ radiometer LST derivation is that it dynamically responds to changing vegetation states in a way that a time limited field campaign cannot.

The Heitronics radiometer is a 'narrow band' sensor and therefore a single central wavelength emissivity value (at 10.8 μm) is sufficient for use in LST derivation. However, the JPL-Apogee based radiometer has a much wider spectral window. Therefore after Cheng et al. (2012) we calculate the hinge point emissivities for the relevant SEVIRI channels, convolved to the Apogee SI series spectral response function. These values are in turn used to calculate the broadband emissivity (BBE) in the spectral range of 8–14 μm (eq. (3)).

$$BBE = 0.2229\varepsilon_{8.7} + 0.67\varepsilon_{10.8} - 0.0152\varepsilon_{12.0} + 0.1045 \quad (3)$$

Here $\varepsilon_{8.7}$, $\varepsilon_{10.8}$ and $\varepsilon_{12.0}$ are the hinge point emissivities for the channels centred at 8.7, 10.8 and 12.0 μm respectively, provided by a LSA-SAF internal product derived from SEVIRI (available from lsa-saf.eumetsat.int). It is noted that although the same emissivity is used in the case of the in-situ and SEVIRI clear-sky LST data, sensitivity of the algorithms to emissivity errors is not the same. Generally, the GSW algorithm is about twice as sensitive to emissivity errors than a method based on the Planck function such as that used here to derive in-situ LSTs (eq. (1)). This is mainly due to the GSW dependence on the average and difference between $\varepsilon_{10.8}$ and $\varepsilon_{12.0}$ (Ermida et al., 2020).

3.2.3. Downwelling correction for surface looking radiometers

To convert the brightness temperature measurements made by the surface viewing radiometers to LST, it is essential to consider the reflected downwelling (full atmospheric path) LWIR component of the measured signal (Göttsche et al., 2016). Whilst a full hemispherical measurement would be the preferred option, a radiometer measurement made at a 53° view zenith angle has been shown to be an appropriate proxy and is easier to achieve in field conditions (Guillevic et al., 2018). This is normally done using a sky viewing LWIR radiometer with the same characteristics as the ground viewing sensor. However, due to an early sensor failure of an Apogee SI-121 radiometer (NASA-JPL radiometer equivalent), until October 2019 only a Heitronics KT15.85 IIP on Mast 3 was observing the sky consistently. Therefore, an estimate of the dowelling radiance had to be obtained from the Heitronics KT15.85 IIP sky measurement that was appropriate to the NASA-JPL radiometers. To do this, 120 downwelling LWIR irradiance spectra were simulated using the radiative transfer model MODTRAN 5 (Berk et al., 2005). These spectra were then convolved to the spectral response functions of both the Heitronics and JPL radiometers to retrieve band-specific downwelling irradiance ($Wm^{-2}sr^{-1}\mu m^{-1}$) values, before being converted to the equivalent sky brightness temperatures (K). The relationship between the Heitronics and Apogee convolved radiances and brightness temperatures were then obtained using linear regression (see S-2 in the supplementary material). Strong positive correlations, $R^2 = 0.99$ and $R^2 = 0.99$ respectively for radiance and BT, were determined for the downwelling observations.

3.2.4. Ground observation uncertainty

Uncertainties on the derived in-situ LSTs were calculated and propagated following GBOV (2018). The uncertainty of any given LST value is a combination of the uncertainty inherent within the logging equipment, the radiometer and the emissivity values applied during LST derivation. The uncertainty of the logging equipment (Uf_{logger}) varies with the temperature of said equipment in terms of both the logger precision (Uf_{l_a}) and logger current resistance (Uf_{l_r}). For the CR300 logger in temperatures below 40 °C the precision values are 0.04 and 0.05 % respectively. For temperatures above 40 °C they are 0.1 and 0.06 % respectively. In addition, the resistors used in the measurement circuit have an uncertainty of 0.001 % (Uf_r). Therefore, the total fractional logging uncertainty is:.

$$Uf_{logger} = \sqrt{\left(Uf_{l\_a}^2 + Uf_{l\_r}^2 + Uf_r^2\right)} \quad (4)$$

The absolute logging uncertainty (Ut_{logger}) in Kelvin is therefore:.

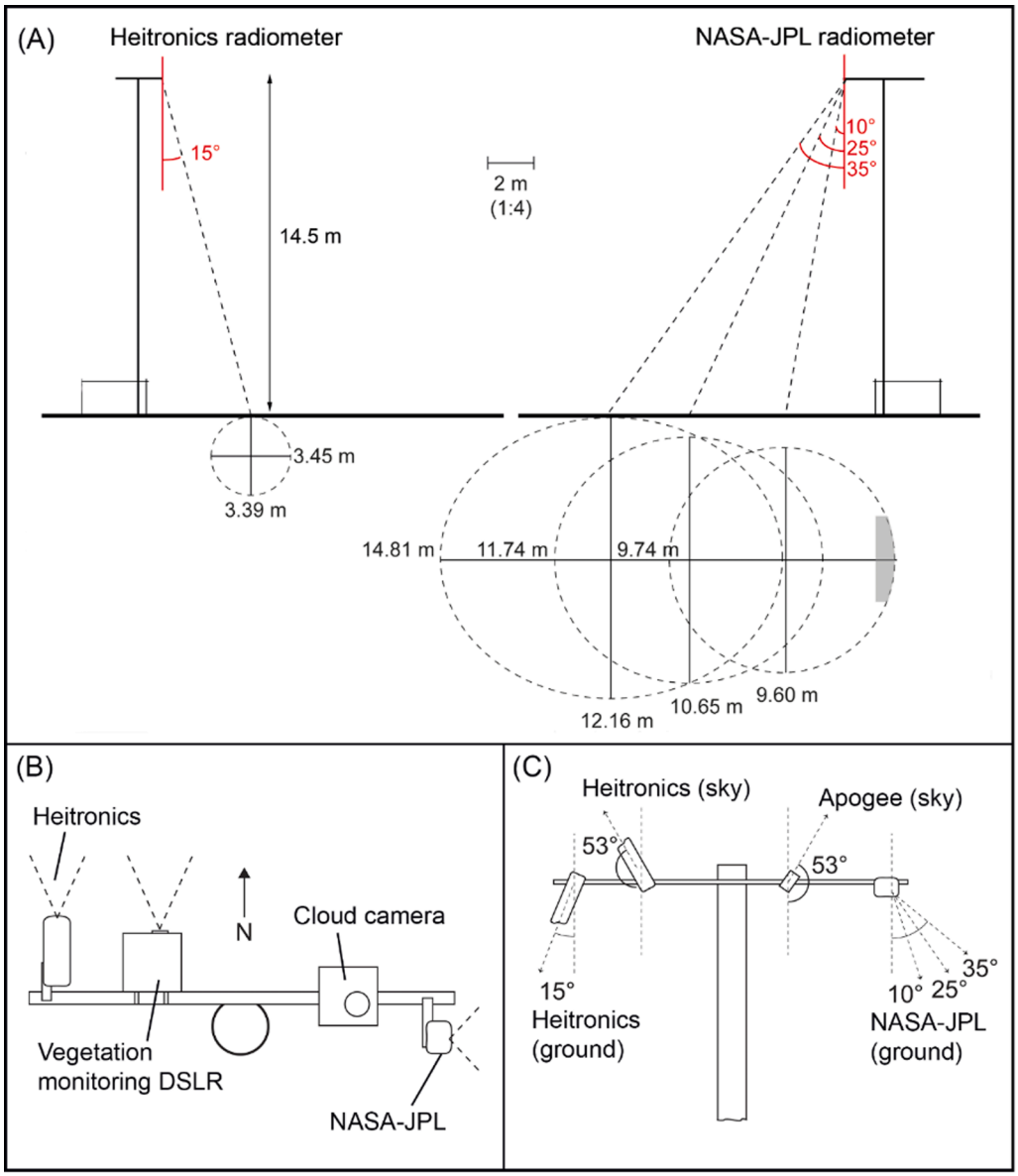

Fig. 3. Panel (A): Sensor FoV geometry for each LWIR radiometer at the given view angles, drawn at 1:4 scale with true angles. The grey box in the 10° JPL radiometer field of view is the region not grazed due to the presence of the fence around the base of the tower. No hardware is present in this region other than the mast. The mast is mounted as far forward in the corner of the fencing as possible to avoid radiometers viewing this area. All digital cameras point north, the same look direction as the Heitronics radiometers. Panel (B): look direction of all sensor types. Panel (C): summary of view angle of all radiometer sensor and observation types.

$$Ut_{logger} = \left(\frac{U_{logger}}{100}\right)T \tag{5}$$

where T = the observed temperature in Kelvin andUf_{l_a}, Uf_{l_r} vary with logger temperature.

Sensor uncertainty (Ut_{sensor}) is provided by both manufacturers. For the NASA-JPL radiometer the stated uncertainty of the sensor is ±0.1 K. For the Heitronics the sensor uncertainty is ±0.5 K plus 0.7% of the difference between the temperature of the sensor body and the temperature of the observed target.

The total observation uncertainty ($U_{T\uparrow/\downarrow}$) in Kelvin is therefore:.

$$U_{T\uparrow/\downarrow} = \sqrt{\left(U^2_{tlogger} + U^2_{tsensor}\right)} \tag{6}$$

The uncertainty of the emissivity is provided by LSA-SAF as part of the SEVIRI product on a per-band basis. Therefore, for the Heitronics sensors the uncertainty in emissivity (U_ε) is the uncertainty of the emissivity for the 10.8 μm channel. However, the JPL radiometer emissivity is driven by multiple channels and therefore from error propagation, U_ε for the NASA-JPL radiometers is:.

$$U_\varepsilon = \sqrt{\left(0.2229U_{\varepsilon_{8.7}}\right)^2 + \left(0.67U_{\varepsilon_{10.8}}\right)^2 + \left(0.0152U_{\varepsilon_{12.0}}\right)^2} \tag{7}$$

where $U_{\varepsilon_{8.7}}$, $U_{\varepsilon_{10.8}}$ and $U_{\varepsilon_{12.0}}$ are the uncertainties for the respective channel emissivities.

Before we propagate these uncertainty values through the LST derivation method, the $U_{T\uparrow/\downarrow}$ in Kelvin must be converted to radiance ($U_{L\uparrow/\downarrow}$, $Wm^{-2}\,sr^{-1}\,\mu m^{-1}$). To do this we differentiate the Planck equation (eq. (2)) with respect to T in order to calculate the equivalent radiance uncertainty for the temperature observation at the true central wavelength for said observation (eq. (8)):.

$$U_L = \left|\frac{\partial B}{\partial T}\right| U_T \tag{8}$$

where U_T = temperature uncertainty in Kelvin and U_L = uncertainty in radiance ($Wm^{-2}\,sr^{-1}\,\mu m^{-1}$) and $\frac{\partial B}{\partial T}$ the partial differential of the Planck function with respect to T such that:

$$\frac{\partial B}{\partial T} = \frac{C_1 C_2 e^{\frac{C_2}{\lambda T}}}{\lambda^6 T^2 \left(e^{\frac{C_2}{\lambda T}} - 1\right)^2} \tag{9}$$

where T = temperature of the observation associated with the uncertainty value (in Kelvin), and constants C_1 andC_2. With all uncertainty contributions accounted for, we can now propagate and find the uncertainty of the land surface radiance ($U_{L_{surf}}$) with the equation supplied by GBOV (2018) (Eq. 8):

$$U_{L_{surf}} = L_{surf} \sqrt{\frac{U_{L\uparrow}^2 + \left((1-\varepsilon)L\downarrow \sqrt{\frac{U_\varepsilon^2}{(1-\varepsilon)^2} + \frac{U_{L\downarrow}^2}{L\downarrow^2}}\right)^2}{\left(L\uparrow - L\downarrow(1-\varepsilon)\right)^2 + \frac{U_\varepsilon^2}{\varepsilon^2}}} \tag{10}$$

Finally, using the uncertainty of the surface radiance ($U_{L_{surf}}$), we calculate the absolute uncertainty of the given LST observation (GBOV (2018) eq. 9):.

$$U_{LST} = C_2 \left(\frac{C_1 \left(\frac{U_{L_{surf}}}{\lambda^5 L_{surf}^2} \right)}{\left(\frac{C_1}{L_{surf}\lambda^5} + 1 \right) \lambda \left(\ln \frac{C_1}{L_{surf}\lambda^5} + 1 \right)^2} \right) \tag{11}$$

where U_{LST} is the uncertainty of a given LST observation given the equipment's operating temperature. The resulting uncertainty for all LST observations at all sites is summarised in Table 2, with the median, minimum and maximum uncertainty values for each radiometer and its angle of observation through time reported. The median uncertainty through time for all radiometers varied between 0.79 and 0.95 K.

3.2.5. Upscaling

The satellite observed LST over any given pixel is a combination of landcover types, landcover structure, viewing angle and illumination angle. The LST observed from a single ground-based radiometer will not include all landcover components and be subject to less shadowing of the surface than the satellite view. Therefore, we upscale the observed LST from each mast to the SEVIRI satellite pixel scale in order to carry out evaluation of the satellite LST product. The workflow for this process as applied to the different illumination conditions is presented in Fig. 4.

For illuminated (day) clear-sky scenes we upscale from ground LST to SEVIRI pixel LST with the Ermida et al. (2014) geometric model, using the observations of sun-lit ground and the tree canopy at Mast 3 as proxy for shadowed surface temperatures. The use of a tree canopy proxy for the shadowed fraction of a pixel follows the approach of Guillevic et al. (2013). S-4 in the supplementary material presents details of testing this method against an air temperature approach. The model requires an estimation of both total tree-cover and the general dimensions of the trees within the SEVIRI pixel. From manual sampling of aerial photos, we estimated crown horizontal radius to range between 3 and 5 m. Field observations indicated that tree heights ranged between 3 and 6 m. For estimating tree canopy cover extent across the site, we used all cloud-free surface reflectance data from the Sentinel-2 Multispectral Imager (MSI) from January and February 2018 over Kapiti Research Station to carry out a supervised classification with a Random Forest classifier. The results of this are presented in Table 3 and shown in Fig. 1. Sentinel-2 MSI samples with a global revisit period of 5 days across 13 spectral bands from the visible to the shortwave infrared with spatial resolutions from 10 m to 60 m depending on the band. Given the relatively short period (six months) considered in this study, we did not update the landcover map through time. However, this would be a necessary step on an annual basis for future work.

The Ermida et al. (2014) model is based on the geometrical optical module of the Geometrical-Optical Radiative Transfer (GORT) model of Ni et al. (1999). The key assumption of this model is that the radiance of a satellite pixel is a linear combination of the radiances from each of the scene components, with each contribution weighted by the respected fraction within the projected scene. It is also assumed that angular variation in observed radiance is solely due to changes of land cover component fractions within the pixel. Thus:.

$$B_{avg} = F_{sunlit} * B_{sunlight} + F_{shadow} * B_{shadow} + F_{canopy} * B_{canopy} \tag{12}$$

where B_{avg} is a pixel's radiance within the sensor field of view,$B_{sunlight}$, B_{shadow} and B_{canopy} are the respective radiances for each component andF_{sunlit}, F_{shadow} and F_{canopy} are the corresponding component fractions as calculated from the landcover analysis and application of the model.

Estimates of the fraction of each component are found using a Boolean Scene Model (Serra, 1982) that finds the gap probability between randomly distributed objects. The density of the object centres is estimated following Liu et al. (2004). Estimations of the fractions of each component are then determined by applying the Boolean scene model to the view and illumination angles of a given pixel on to a 0.01 m regular grid with an ellipsoidal tree. For full details of the model see Ermida et al. (2014).

As we are using the tree canopy temperatures as a proxy for canopy shadow temperatures, the function to scale the ground observations becomes:.

$$B_{avg} = F_{sunlit} * B_{grass} + \left(F_{shadow} + F_{canopy}\right) * B_{canopy} \tag{13}$$

where B_{grass} is the radiance from the radiometer observing the grass-soil surface at each mast. During the day, the fractions are driven by the modelled shadowed fraction to give B_{avg}. At night and under cloud cover there is no illumination of the scene and therefore the fractions are set to the estimated tree canopy cover (6%) and vegetation surface (94%) of the pixel in which the masts are located. Given that we are only looking at one full season, we do not update the landcover map during the course of this time period. Thus, the implementation for observations at night (Bn_{avg}) is:.

$$Bn_{avg} = 0.94 * B_{grass} + 0.06 * B_{canopy} \tag{14}$$

Due to the location of Kapiti close to the equator, 'Day' is set to 0300 – 1500 UTC and night vice versa. With the average brightness temperature calculated, eq. (1) is applied to find the up-scaled ground validation LST temperature for the SEVIRI pixel in question. The upscaling of ground observations for the validation of MLST-AS is carried out for each individual mast, based on the SEVIRI view angle and azimuth for Kapiti. The final step is to then find the Kapiti site mean, which is the mean of all the time-matched mast upscaled observations that are oriented in the same direction as the SEVIRI view angle (east). By taking

Table 2
Summary statistics for the calculated LST uncertainty values for each site and sensor/observation type. All values are in Kelvin.

Site	Radiometer observation	Median	Min	Max
1	Heitronics	0.79	0.50	1.78
	JPL 1	0.91	0.49	1.81
	JPL 2	0.91	0.47	1.80
	JPL 3	0.91	0.47	1.80
2	Heitronics	0.81	0.50	1.49
	JPL 1	0.96	0.49	1.78
	JPL 2	0.95	0.47	1.78
	JPL 3	0.95	0.47	1.78
3	Heitronics (tree)	0.88	0.50	1.82
	JPL 1	0.92	0.48	1.82
	JPL 2	0.92	0.47	1.85
	JPL 3	0.93	0.48	1.83
4	Heitronics	0.91	0.50	1.84
	JPL 1	0.94	0.49	1.80
	JPL 2	0.94	0.47	1.80
	JPL 3	0.93	0.48	1.80

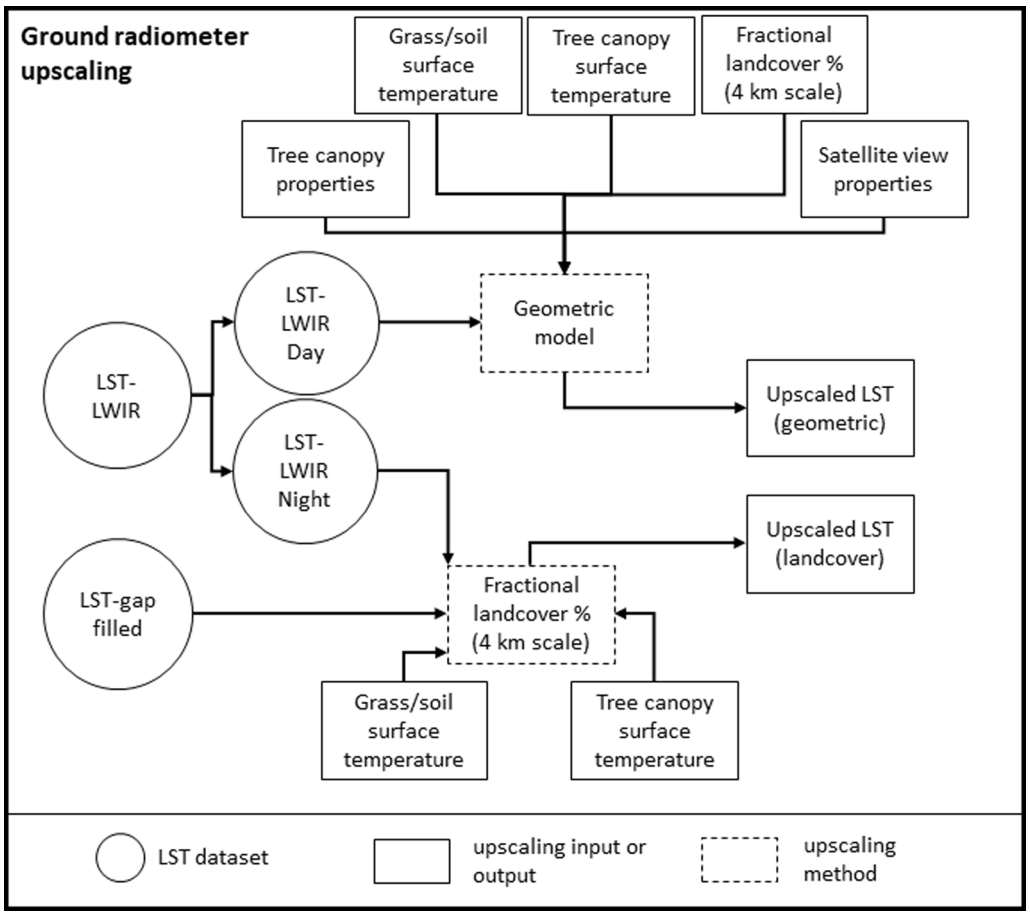

Fig. 4. Upscaling workflow for ground observations to the pixel resolution of SEVIRI MLST-AS. Day and cloud-free ground LST observations are upscaled using the geometric model. Night and cloud shadowed ground observations are upscaled using a simple landcover fraction-based combination of the tree canopy and grass/soil surface temperatures due to the lack of shadows.

Table 3
Summary table of average percent landcover within SEVIRI pixels undergoing LST comparison to Kapiti ground stations. Rand accuracy = 0.97, indicating that 97% of test pixels are classified correctly using the model found by the evaluation of the training pixels.

Class	Land cover (%)
Tree canopy	6.0
Other vegetation	82.6
Surface water	0.2
Exposed soil	11.2

the mean ground observed LST across multiple masts we sample the impact of the three different grazing patterns across Kapiti by an equal amount.

3.3. Validation metrics

For clarity, the following definition of validation metrics are used throughout this work, adopted from Guillevic et al. (2018):.

(5) Accuracy: the median error of the satellite product as compared to the ground truth provided by the Kapiti LST validation towers:

$$\text{Accuracy} = median(|x - y|) \tag{15}$$

where x is the observed ground LST value and y is the time-matched satellite LST value.

(ii) Uncertainty: estimated by the RMSE:.

$$RMSE = \sqrt{\frac{1}{n}\sum_{i=1}^{n}(x_i - y_i)^2} \tag{16}$$

where n is the total number of observations, i is a whole positive integer that enumerates sum, x is the observed ground LST value and y is the time-matched satellite LST value.

(iii) Precision: the median of the absolute deviation (MAD) of each measurement's error from the median error of the whole dataset:.

$$MAD = median(|z_{i=1} - \tilde{z}|) \tag{17}$$

where z is the difference between x andy, i is a whole positive integer that enumerates the series of z and $\tilde{z}$ is the median of z.

iv) Slope: a description of the direction and steepness of the linear best fit between the in-situ and satellite LST measurements as found using an ordinary least squares regression. It is a useful indicator of the general representativity of the whole range of satellite observed temperatures with regards to the whole range of in-situ temperatures.

4. Results

4.1. In-situ data record

Fig. 5 summarises the stable data record for site configuration 1. Some operational issues were encountered that affected the available record; Mast 2 had all power equipment stolen shortly after installation and Mast 3 was badly damaged by a curious giraffe. The outcome of this

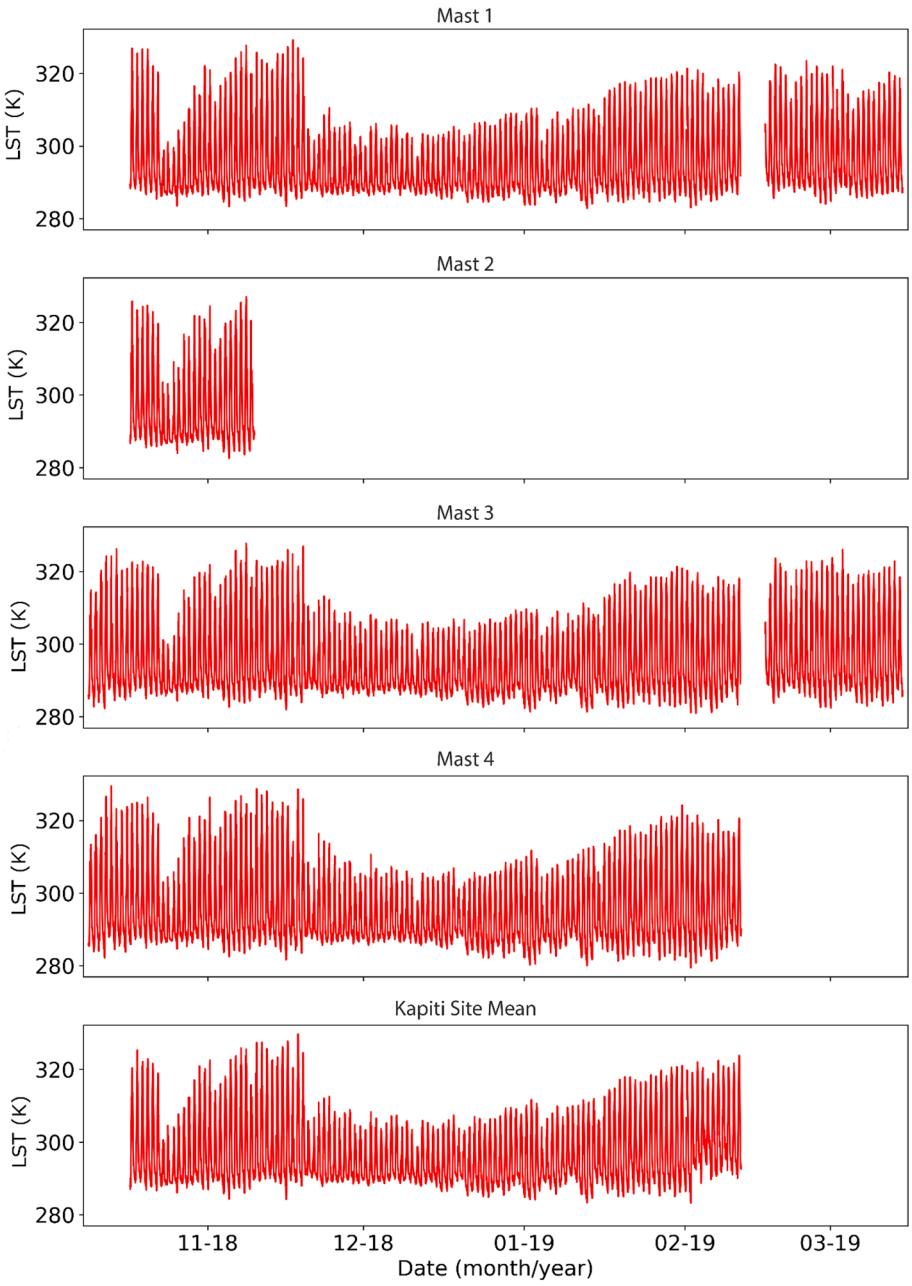

Fig. 5. Summary of the available in-situ LST record (Kelvin) for Kapiti site configuration 1 and the processed Kapiti-wide upscaled mean LST. Data is available from a mast when at least one ground observing radiometer is active and returning admissible data. The Kapiti Site mean is only available when at least three radiometer observations are available from two masts. The timeseries presented in the top four panels are the downwelling and emissivity corrected LST values for each mast upscaled to the SEVIRI pixel scale. The final timeseries is the Kapiti mean LST derived from all four sites and upscaled to the SEVIRI pixel scale. The data gap in late January 2019 at a number of sites is due to batteries failing from repeated charge/discharge cycles.

is that in the first full year of operation, the instruments installed at Kapiti research station capture one full wet-dry seasonal cycle across three masts. This three mast timeseries suffers one data gap of approximately seven days due to power failure at two of the masts. We therefore have a total observation period of ~6 months. A full record of the individual radiometer ground observations is presented in S-5 in the supplementary material. The ground LST value taken forward into the evaluation of MLSTS-AS is the Kapiti site mean (Fig. 5- last plot). Observations between the satellite and the ground are matched if they occurred within 30 seconds of one another.

4.2. MLST-AS

Fig. 6 demonstrates the performance of the all-weather MLST-AS product against Kapiti in-situ observations. Taken as a whole, the MSLT-AS has an accuracy of 2.02 K, precision of 1.38 K and an RMSE of 3.64 K, with a slope of 1 (Fig. 7-A). However, the two methods used to derive the all-weather MLST-AS product show different levels of performance and structure. The energy balance model (Fig. 6-B) component of the MLST-AS product shows a poorer performance, with an accuracy of 3.02 K and RMSE of 4.16 K, and there is a clear cold bias present in the primary cluster of values. Fig. 6-C demonstrates that the GSW-derived SEVIRI LWIR LST (also known as the MLST product) of the LSA-SAF product is generally accurate over the sparse canopies of the savannah, with the exception of a lower spur of cold-biased values. that are likely the result of small clouds missed by the cloud filter.

To further investigate the difference in performance between the two contributing elements of MLSTS-AS, in Fig. 7 (panel A) we examine the daily bias and MAD values for the MLST-AS product against the upscaled Kapiti in-situ LST with a rolling 7-day mean. In Fig. 7 panels (B) and (C) the data from the MLSTS-AS product is split into the two elements: first the observations from the clear sky LWIR SEVIRI and secondly those derived from the energy balance model at times of cloud. Both methods of LST derivation experience the occasional severe outlier

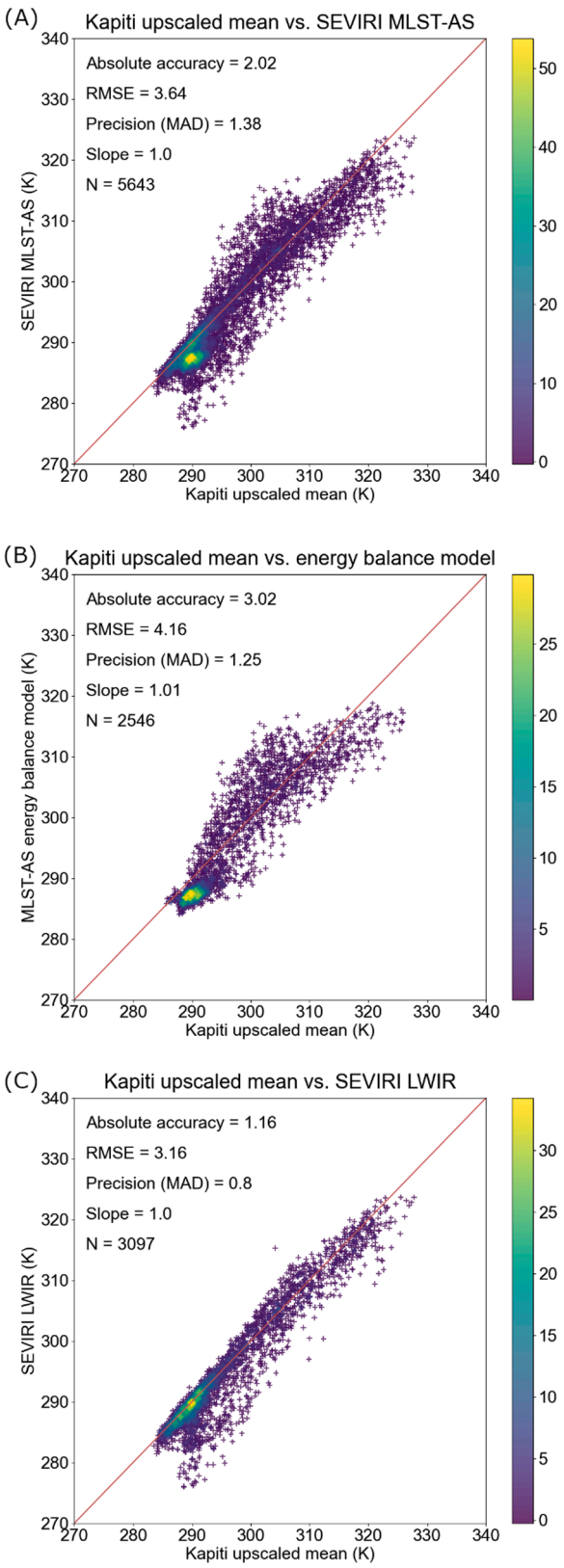

Fig. 6. Mean upscaled Kapiti in-situ LST against (A) the new SEVIRI all-weather MLST-AS product as a whole, (B) the energy balance model component of the MLST-AS product (at times of cloud), and (C) the standard SEVIRI LST LWIR product. The colour bar in each panel is the number of observations located at that point in the 2D plain. The 1:1 line is shown in red on each plot, and the slope of the ordinary least squares line of best fit to the data is provided as one of the statistics.

(errors greater than 4 K), with the energy balance approach suffering approximately double the number of these compared to clear sky GSW observations. An interesting difference between the MLST-AS pixels derived with the energy balance model (cloudy pixels) and those derived with the GSW (clear sky pixels) is the change in phase of the errors. The precision and bias are in phase throughout the wet and dry seasons for the surface temperatures derived using the energy balance model. However, the relationship between the bias and precision in the clear sky measurements switches to an anti-phase/neutral configuration following the end of the wet season. This suggests that the model response to surface water and vegetation cycling is different to that of the satellite LST observation derivation.

To explore these discrepancies in detail, Fig. 8 examines MLST-AS for six days commencing 20th October 2018, presenting the daily LSTs from in-situ and MLST-AS observations in panel A and cloud conditions and meteorological measurements for dry/scattered cloud and full cloud cover in panels B and C respectively. If the surface temperatures were to be examined alone, this week might be thought to be the start of the rainy season as there are three days of increasingly cloudy conditions before the surface temperature drops on the 23rd and 24th October. Skies are clear at night in the build up to the drop, with progressively more cloud present in the day. As we get closer to the temperature shift, the LSTs derived using the LWIR observations of SEVIRI at times of cloud free skies become more infrequent and less accurate. From the 23rd onwards there are almost no clear sky observations, and the energy balance model becomes almost the sole provider of LST data within MLST-AS, with just one or two cloud-free points available in a 24-hour period. There is also a distinct difference between the performance of the MLST-AS product at the start of the week (clearer-sky conditions) and the end of the week (cloudy conditions). On the 20th and 21st October there is fairly good agreement between the in-situ LSTs and the MLST-AS product both in terms of diurnal pattern and bias, with the MLST-AS LSTs generally within 2 K of the in-situ upscaled LSTs. Some negative biases down to −5 K and even −10 K at 05:35 UTC on 20 October 2021 suggest cloud contamination. From 08:00 UTC on the 22nd of October, we see an immediate and large drop in MLST-AS performance (Fig. 8, panel A). There also emerges a consistent pattern of the MLST-AS having a positive bias during the day and large negative bias during the night when compared to the in-situ LSTs. Differences are maximal in the middle of the day and during the night, with differences peaking at + 6.5 K during the day and −14 K during the night.

This immediate and large drop in both in-situ and satellite LSTs from the morning of the 23rd October (Fig. 8, panel A) suggests that a key factor to influence the surface temperature in cloudy conditions is heavy dew formation in the mornings. Fig. 8C indicates that no precipitation is recorded, and relative humidity maintains a daily cycle that is in-sync with the surface temperature as it did a few days earlier during dry and cloudy conditions (Fig. 8B). However, Fig. 8C shows that on the 23rd October the soil temperature drops away from surface temperature. When also considering the dew evident in the cloud camera images, these observations suggest heavy and persistent dew formation that changes the thermal properties of the surface in a way that cloud-cover alone cannot account for. The amount of dew is not sufficient to infiltrate the compacted upper surface of the soil nor is there enough to run off the surface and into the cracks to change the soil moisture levels.

Fig. 9 shows similar data to Fig. 8, but for six days commencing 18th November 2018. In this week, the true onset of the rainy season is evident from a clear precipitation signal (Fig. 9- panel C) on 19th November. This rainfall is matched by strong evidence of infiltration into the soil immediately during and after the precipitation event, with rapid and large changes in both soil moisture and 5 cm soil temperature. Relative humidity and soil temperature follow the same pattern as in Fig. 8 as they are in-sync with the observed LST before water is on the land surface, followed by soil temperature dropping away once moisture is on the surface. As in Fig. 8, when water is on the land surface, MLST-AS modelled temperatures appear to overestimate daytime temperatures

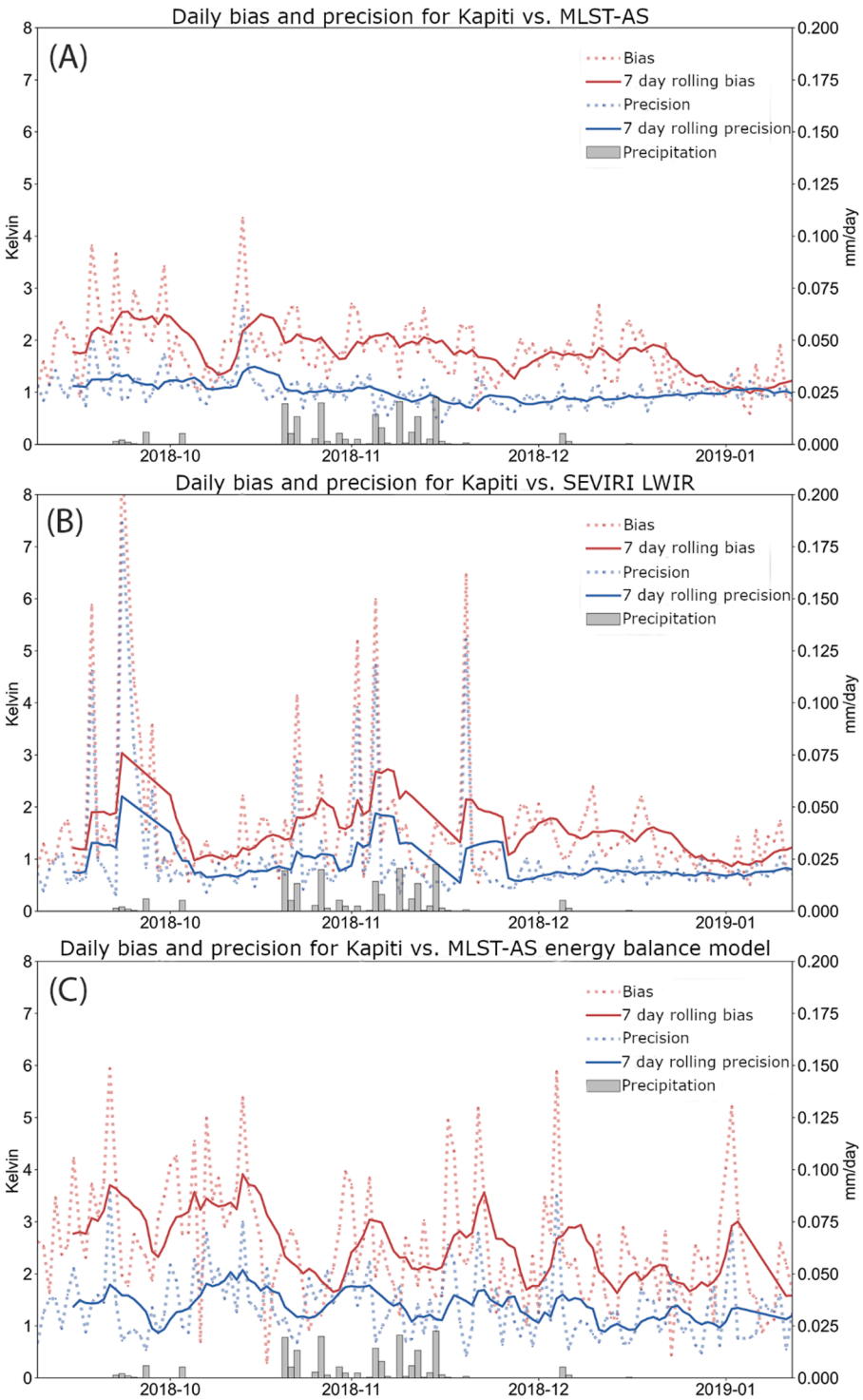

Fig. 7. MLSTS-AS error statistics through time. Panel (A) daily mean bias (absolute) and precision with a 7-day rolling average applied, for the full MLST-AS product. (B) Daily mean bias (absolute) and precision with a 7-day rolling average applied, for the clear sky thermal infrared observations of SEVIRI within MLSTS-AS. (C) Daily mean bias (absolute) and precision with a 7-day rolling average applied for the cloudy periods in which the MLST-AS product is providing LST values for Kapiti using an energy balance model. For all plots, the left axis is the absolute bias and precision in Kelvin. The right axis is the daily precipitation in mm. Dashed lines are daily mean bias/precision, the solid line is the 7-day rolling mean of this daily bias/precision. Grey bars are the daily precipitation total, provided to indicate the wet season.

and significantly underestimate night-time temperatures when compared with the in-situ measurements. MLST-AS temperatures then close in with the in-situ observations once surface water is no longer present, or soil moisture decreases below saturation levels. There is also a general pattern in this scenario of the night-time energy balance modelled temperature values being consistently offset from the in-situ observations.

Fig. 10 shows the hourly (UTC) summary statistics for the upscaled in-situ measurements against the MLST-AS product, considering accuracy, precision, RMSE, and slope for each component of the MLST-AS product. Consideration of the whole MLST-AS product (Fig. 10- panels A, D, G) against the Kapiti upscaled mean indicates that the RMSE and precision error is lowest around dawn (03:00 UTC) and dusk (15:00 UTC), with RMSE and precision both getting worse during the day towards solar maximum (~10:00 UTC) before improving as dusk approaches. This pattern of changes in the magnitude of uncertainty and error over the 12-hour cycle between dawn and dusk is also observed during the night, albeit in both cases the decrease in RMSE and precision performance is less than during the day.

The model component and the clear-sky component follow similar patterns of precision and RMSE to the whole MLST-AS product. However, while the model component has a similar distribution of poor slope

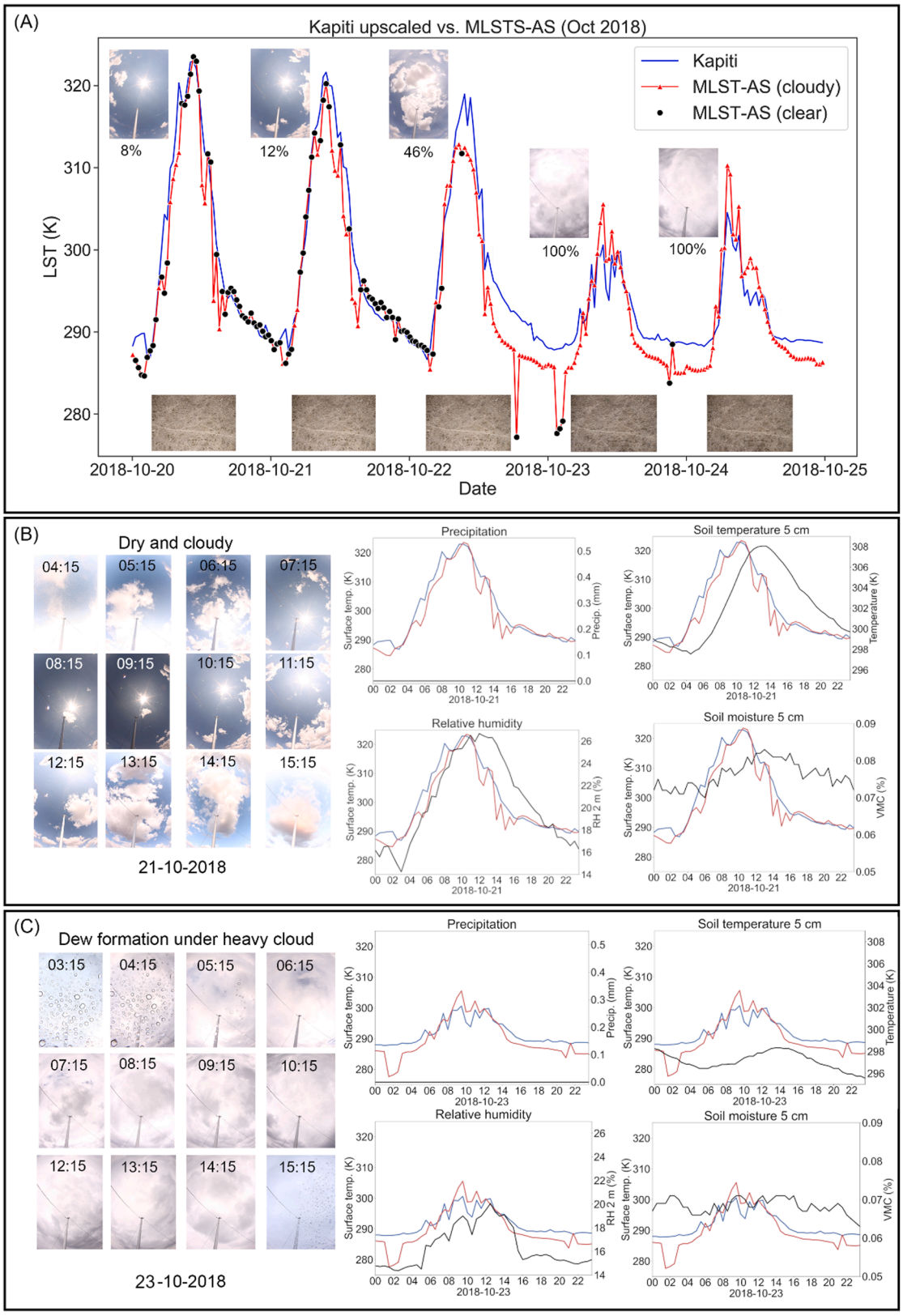

Fig. 8. (A) Time-series of LST data for October 2018, at the onset of dew formation. Blue = Kapiti upscaled mean in-situ LST. Red = MLST-AS product, with red triangles the LST values provided by the energy balance model. Black = MLSTS-AS LST from a clear sky observation of the ground by SEVIRI. A daily cloud camera image at 10:15 UTC is shown from the camera mounted on Mast 3, with cloud fraction indicated. (B) Hourly sky images from the afore-mentioned cloud camera and environmental parameter plots for a dry and cloudy day without dew formation (21/10/2018). In all plots the time is in UTC, the red line is the MLST-AS record, blue is the upscaled Kapiti ground observation (both on the left y-axis) and black is the given environmental parameter (right y-axis). (C) Hourly sky images and environmental parameter plots for a day with morning dew formation under heavy cloud (23/10/2018). The unit of soil moisture is the volumetric moisture content (VMC).

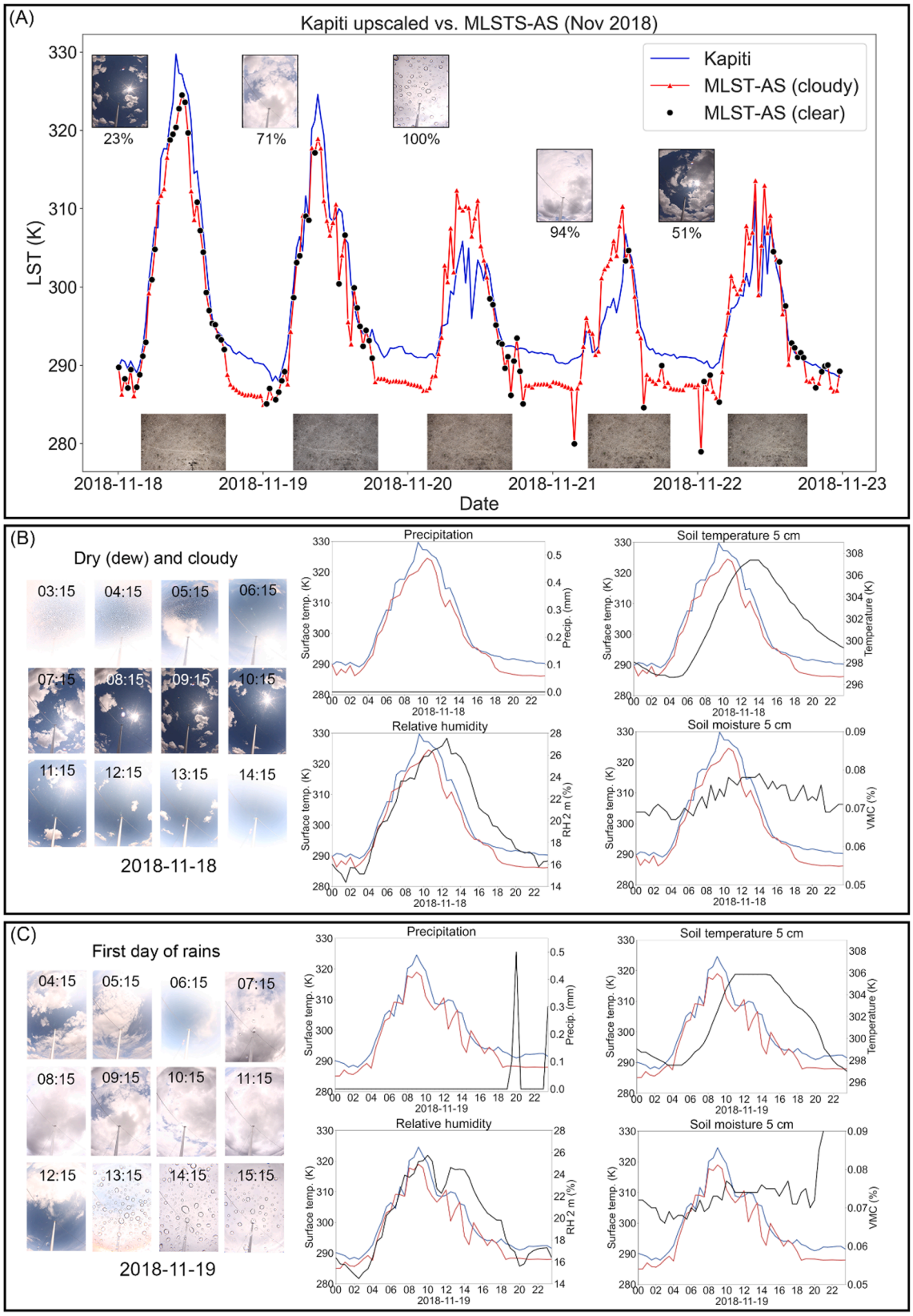

Fig. 9. (A) Time-series of LST data for November 2018, the start of the rainy season. Blue = Kapiti upscaled mean LST. Red = MLST-AS product, red triangles are the LST values from the energy balance model. Black = MLSTS-AS LST clear sky observation by SEVIRI. Similar to Fig. 8, a daily cloud camera image at 09:15 UTC is shown from the camera mounted on Mast 3, with cloud fraction indicated. (B) Hourly sky images and environmental parameter plots for a dry and lightly clouded day. In all plots, time is in UTC, the red line is the MLST-AS record, blue is the upscaled Kapiti ground observation (both on the left y-axis) and black is the given environmental parameter (right y-axis). (C) Hourly sky images and environmental parameter plots for first day of rains, which commence in the evening. The unit of soil moisture is the volumetric water content (VMC).

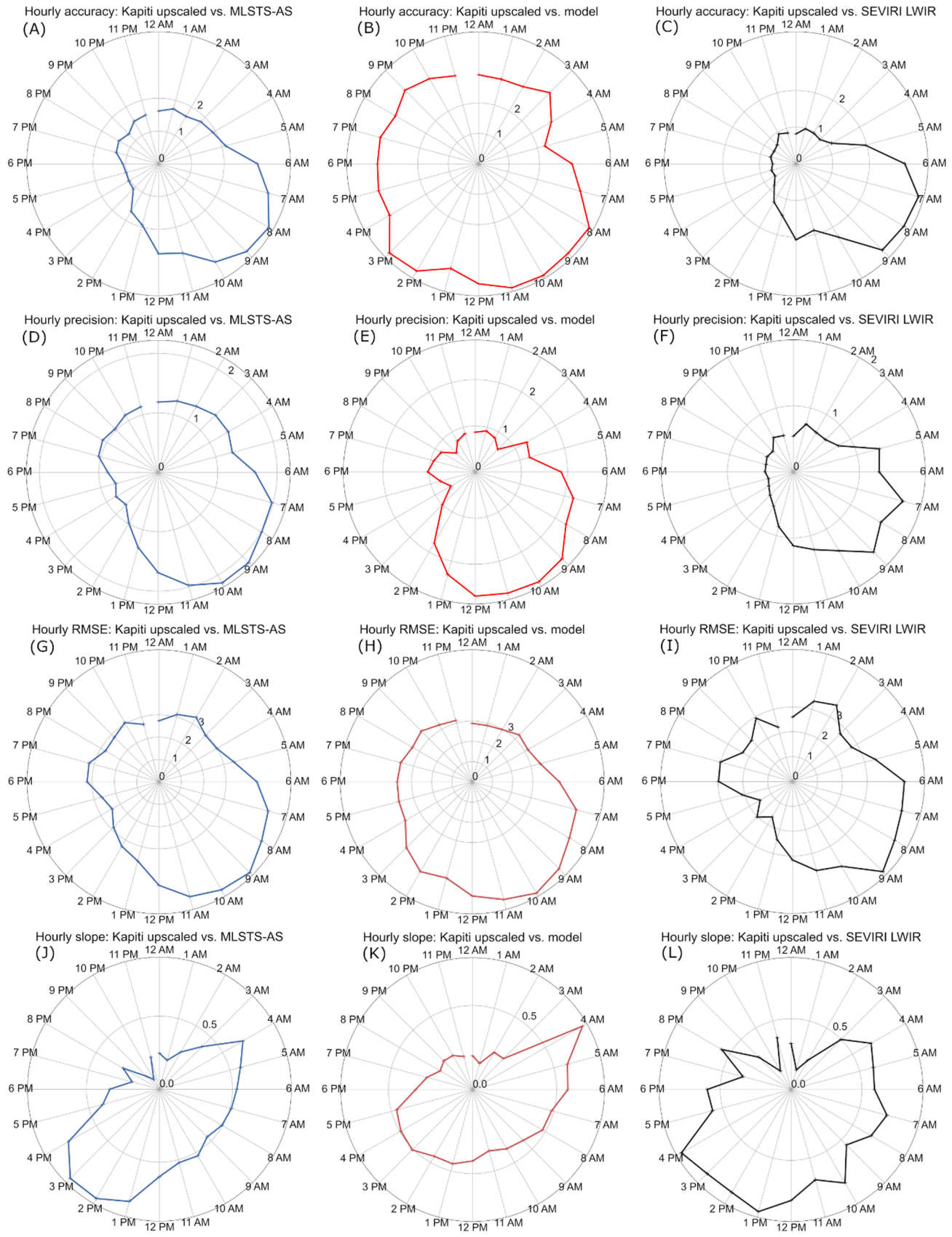

Fig. 10. Hourly (UTC) summary statistics for Kapiti mean vs. MLST-AS, from top to bottom; accuracy, precision, RMSE and slope. Blue plots (A, D, G, J) are for the whole product, red plots (B, E, H, K) are for the model component only and black plots (C, F, I, L) are for the LWIR component. The values given are the evaluating statistic for all values in the timeseries, for that given hour of the day. For local time, add three hours to the given UTC time. For the first three statistics the x-axis goes from 0 to 4 and is in Kelvin, for slope the x-axis is from 0 to 1.

fitting during the night to the clear-sky component, the overall fit is much poorer on an hourly basis as compared to the LWIR observations (Fig. 10- panel K and L). In addition, the accuracy of the model component is much worse than that of the clear-sky component and the whole MLST-AS product (Fig. 10, panels A – C), with the exception of the hours preceding the solar maximum (07:00 – 09:00 UTC).

5. Discussion

5.1. MLST-AS performance

The overall results of the MLST-AS product (accuracy = 2.02 K, precision = 1.38 K and RMSE = 3.64 K) are close to the GCOS (2016) target of < 1 K accuracy and precision for LST products and consistent with the findings of Martins et al. (2019) and Martins & Dutra (2020). However, the results from the comparison presented in Section 4.2 suggest a number of issues with the MLST-AS product.

Firstly, there is clear evidence of cloud detection issues with the SEVIRI LST algorithm. The first evidence of this is the lower spur of cold-biased values observed in the GSW-derived LSTs (Fig. 6C), which are likely the result of small clouds missed by the cloud filter. Considering Fig. 8A and Fig. 9A, it can be seen that these large negative biases occur mostly during night-time when the cloud masking algorithm cannot rely on the visible channels, which makes the correct detection of clouds much more difficult. We can also see this clearly in Fig. 10- panel L where the slope of the fit between the SEVIRI LWIR and ground data drops suddenly from close to 1.0 at 4 PM UTC (nightfall) to less than 0.1 by 12 AM (pre-dawn). Interestingly, as shown in Fig. 7, these occasional high biases and poor precision values are observed in both the model component and the clear-sky component. Cloud-detection errors for the LWIR observations likely are the cause of this, as the MLST-AS energy balance model is linked to the LWIR observations.

However, cloud-detection errors alone do not account for the apparent underestimation of night-time temperatures observed consistently in cloudy conditions when dependent on the model component alone (Figs. 8 and 9). Cloud-detection errors do also not explain the apparent overestimation of daytime temperatures in cloudy conditions as observed in Figs. 8 and 9. This pattern of underestimation at night and overestimation at day during cloudy conditions was similarly observed by Martins & Dutra (2020). An alternative explanation for these errors is likely insufficient characterization of soil moisture, which is known to be an issue for the MLST-AS energy balance model due to a lag in the soil moisture data that feeds surface temperature derivation (Ermida & Trigo, *pers. comm.*). This is supported by the fact that the model response to surface water and vegetation cycling was observed in Fig. 7 to be different to that of the satellite LST observation derivation. Based on this and the ground data shown in Figs. 8 and 9, we therefore suggest that if soil moisture comes to strongly control surface temperatures and there are few clear sky LWIR observations to correct the model, the model fails to represent the diurnal cycle well.

These issues around the energy balance model capturing soil and surface moisture conditions could also be the cause of the diurnal changes in the magnitude of uncertainty and error observed in Fig. 10 (panels B, E and H) and presented in Section 4.2. However, this is thought to be unlikely as both elements of MLST-AS experience the same pattern of warmer surface temperatures leading to a performance against the ground stations that is 1–2 K worse than in the morning or night (Fig. 10- panels A to I). Therefore, it is suggested that there are two elements of the savannah biome that both the energy balance model and SEVIRI LWIR observations are struggling to deal with: 1) surface water deposition and subsequent soil moisture levels and 2) higher surface temperatures (>300 K (Fig. 6)).

Surface water could drive errors in the MLST-AS LST due to changes that it may cause on land surface emissivity (LSE) as observed by both the satellite and the radiometer (Mira et al., 2007). The FVC derived emissivity of the LSA-SAF product will not capture the impact of saturated soils nor a film of water on said LSE. The effect could be the same for both the in-situ radiometers and the satellite, but due to the difference in scale it is more likely to be a differential influence. The differential in the effective LSE experienced by each sensor would occur as water will gather in discrete locations (the dry stream beds and watering holes) at the larger landscape scale, whereas in the view of the radiometers it is much more likely to be present as a film through which vegetation is still visible. This generates a different LSE through both the type of material observed (water vs. mixed water and vegetation) and differences in surface roughness. However, Hulley et al. (2010) found in laboratory experiments that LSE returned to the dry equilibrium state just an hour after wetting. They also found minimal impacts of anomalous wetting events over desert environments, particularly when the split-window algorithm is used and LSE forced to a pre-determined constant for the observed landcover (Hulley et al., 2010). Furthermore, given that we see the large bias over the whole course of a night with a far more minimal difference than in the day, it is unlikely that a surface water driven change in LSE is the primary cause of the general error and highly unlikely to be the cause of the night-time bias. This is because if it was an LSE driven bias, we would expect the same bias to be present in the day as at night, given that the emissivity of a surface is independent of solar illumination and that the angle of observation remains constant for both the satellite and the radiometer (Li et al., 2013).

5.2. Limitations and future work

There are three areas in which this study has limitations that require further study: i) emissivity, ii) upscaling evaluation and iii) grazing representativity.

Emissivity remains the most difficult element of the LST validation process to constrain. By using the FVC derived emissivity that is part of the SEVIRI LST product we do, to some degree, neutralise it as a source of comparative error between the satellite and ground observations. However, as explored in Section 5.1 this means that we cannot give a definitive answer as to the mechanism of the role that surface water has in the observed cold bias of MLST-AS. This is because we have no measure of the 'true' emissivity as experienced by the ground radiometers when the ground is wetted as compared to when it is not. Some work was carried during the course of this project with the box method of Rubio et al. (2003) to rectify this but the approach was found not to be suitable for the savannah environment (Langsdale et al., 2020). Future work should include a concerted field campaign with instruments such as the Cimel 312 as used by Payan and Royer (2004), to build a spectral library of the savannah biome through both the wet and dry seasons. This would be logistically difficult but allow the potential source of error to be identified and quantified should it be emissivity based.

In addition to measurements of emissivity through time, another limitation of this work is the evaluation of emissivity at different scales. To paraphrase Zhang et al. (2004): "the concept of scale in thermal measurements is a purely human construct due to the limitations of measurement capabilities, in the natural world heterogeneity is absolute throughout the scale continuum". This said, scale is still an issue that must be tackled given that the difference between our sensors is so large: a 4000 m measurement for SEVIRI vs. 3 m in the case of the Heitronics. We mitigate this scale difference somewhat by measuring each component of the landscape on the ground with multiple radiometers, rather than the whole landscape with one radiometer. But there is still a challenge around the respective contribution of each landscape element to the emissivity of the observed surface. For example, we do not provide a different emissivity for the tree canopy as compared to the grass canopy in the radiometer LST derivation. Nor are we able to define the relative proportion of soil to grass that is visible in the FoV of each radiometer that is looking at the grassland. Both of these factors could have an impact on the true emissivity that should be used with the ground radiometers, albeit research indicates that trees are graybodies once they reach a sufficient total canopy depth and leaf density

(Meerdink et al., 2019a, 2019b). As with the problem of surface water, a concerted yearlong ground campaign would do much to answer these questions. A fuller answer could be gained by a campaign of robust, ground emissivity measurements that is then combined to machine learning based quantification of the soil-grass component balance via the vegetation monitoring DSLRs.

The second limitation of this work is the lack of an evaluation of the upscaling effectiveness. The Ermida et al. (2014) model has been widely used and is the same as that used at the Evora site. However, as with emissivity we lack an objective 'truth' against which to test the performance of the model in upscaling our component temperature observations to the satellite scale. There are two possible approaches that could be applied in the future to rectify this. Firstly, the use of intermediate scale sensors to provide check points against which to compare the scaling effort and secondly through a further modelling step. In the first instance this could take the form of two intermediate scale datasets from a drone mounted sensor (e.g., Desai et al., 2021) and then the ECOsystem Spaceborne Thermal Radiometer Experiment on Space Station (ECOSTRESS) sensor (Hulley et al., 2021). In the second case, the approach of Li et al. (2019) would provide a powerful tool for the evaluation of both upscaling effectiveness and the general representatively of our component temperature measuring effort. However, further sensor installations would be required, and the aforementioned emissivity evaluation field campaign conducted in order for this to work.

The upscaling does also not take into account discrepancies in cloud cover between the different ground stations and the satellite scale. It is possible that small clouds generate local drops in temperature of different magnitudes at different masts that are not representative of the satellite scale, and in some cases so small as to not even be detected by the cloud-detection algorithm within the LWIR product. A first step towards understanding these disparities would be to add cloud monitoring cameras to all masts.

Finally, whilst we do capture some of the impact of the different grazing patterns across the SEVIRI pixel through our placement of masts in locations that capture the primary three grazing levels, we assume that all three are present in equal amounts. This is quite a broad assumption given the mixture of both managed and wild animal grazing that occurs across the whole ranch. In order to resolve this, we would need to create a detailed and dynamic grazing map of the SEVIRI pixel. This is possible through a combination of field surveys, drone surveys and automated classification tools. Such a survey would also allow the creation of a higher resolution landcover map than is currently available, which would also greatly enhance the upscaling effort.

6. Conclusions

In this paper we have described a new satellite LST product validation facility located at ILRI's Kapiti Research Station (Kenya). The station is the first of its kind in East Africa and it possesses sufficient infrared radiometers to be confident of capturing surface LST heterogeneity in a savannah biome. The site also benefits from contextual environmental sensors in the form of vegetation monitoring cameras and an eddy-covariance-meteorology station to aid in the identification of sources of error. To our knowledge, this is the first time this has been achieved for an African savannah in the context of LST validation. The evaluation of satellite LST products made with data from this new station represents a step-forward in terms of LST product validation for East Africa and for surface temperatures strongly influenced by sparse seasonal vegetation canopies.

We use the ground data from Kapiti site to evaluate the new all-weather MLST-AS product. The key findings of this validation effort are:

- The new MLST-AS, an all-weather LST product for the full disk, has an overall accuracy of 2.02 K.
- MLST-AS suffers from a previously unidentified night-time cold bias when surface water from dew formation or rainfall is present.

In detail, the LSA-SAF all-weather product (MLST-AS) has a precision of 1.38 K, a RMSE of 3.64 K and a slope of 1.0. The LWIR derived LST of the SEVIRI sensor onboard MSG has accuracy of 1.16 K, RMSE of 3.16 K and a precision of 0.8 K with a slope of 1.0. The performance of the energy balance model component of MLST-AS is found to be not as good, with an accuracy of 3.02 K, an RMSE of 4.16 K, precision of 1.25 K and a slope of 1.01. The cold bias (typically 3–4 K) identified in night-time temperatures, occurs when surface water is present. This is probably because of difficulties posed to a model by the presence of a thin film of water that acts as an insulator between the air and land surface, but which is not easily detectable or modelled. There are also clear issues with the cloud-masking algorithm, with cloud contamination resulting in cold biases in the clear-sky product.

The work done here does not answer the question of what is the most appropriate surface emissivity to assume in LST retrievals for the type of vegetation canopy-soil complex present at Kapiti. Nor were we able to tackle the impact of canopy density and senescence cycling on LST validation in terms of either observation angle or emissivity. These are the greatest weakness of the current LST validation approach as a whole and should be the focus of future work. In addition, better constraints need to be placed on the bare soil component when upscaling ground radiometer observations to the satellite scale.

Description of author's responsibilities

This work was conceived and planned by: Dowling TPF, Wooster MJ, Trigo IF, Hook S and Merbold L. Funding for the work was acquired by Wooster MJ and Merbold L. Calibration and construction of radiometers was carried out by: Dowling TPF, Langsdale MF, Rivera G and Hyll K. Site planning, sensor set up, site maintenance and electronics installation was carried out by: Dowling TPF, Main B, O'Shea F, De Jong MC, Nguyen H, Gluecks I, Leitner S and Merbold L. Emissivity ancillary experiments were carried out by: Dowling TPF, Main B, O'Shea F, De Jong MC, Nguyen H and Langsdale MF. Field and satellite LST data acquisition and handling was carried out by: Dowling TPF, Langsdale MF, Ermida SL, Nguyen H, Leinter S, Merbold L and Gluecks I. Geometric illumination modelling was carried out by Ermida SL. LST processing and experiments were carried out by: Dowling TPF, Langsdale ML and Ermida SL. The manuscript was written by Dowling TPF, Langsdale ML and Ermida SL, with input from all other authors. Wooster MJ and Trigo IF provided supervision and management of the whole research and writing process.

Declaration of Competing Interest

The authors declare that they have no known competing financial interests or personal relationships that could have appeared to influence the work reported in this paper.

Acknowledgements

The authors wish to thank in particular all the staff at ILRI Nairobi and ILRI Kapiti Research Station. Without the help of laboratory staff, farmhands, and the security team this research would not have been possible. Stuart Barden (Ausquest Ltd.) is also thanked for allowing the installation of a mast in his farm as part of future work plans. The work was conducted as part of the Pest Risk Information Service (PRISE) project, which is funded from the UK Space Agency's International Partnership Programme (IPP). IPP is a five-year, £152 million programme designed to partner UK space expertise with overseas governments and organisations and supported by the Department for Business, Energy, and Industrial Strategy's Global Challenges Research Fund (GCRF). Elements of the equipment installed at Kapiti were funded by NERC National Capability funding though the UK's National Centre for Earth Observation (NCEO; NE/R016518/1). Ilona Gluecks, Sonja Leitner and Lutz Merbold acknowledge the CGIAR Fund Council, Australia

(ACIAR), Irish Aid, European Union, International Fund for Agricultural Development (IFAD), Netherlands, New Zealand, UK, USAID and Thailand for funding to the CGIAR Research Program on Livestock. Final thanks must go to Emma Olley for data recovery.

Appendix A. Supplementary material

Supplementary data to this article can be found online at https://doi.org/10.1016/j.isprsjprs.2022.03.003.

References

Abrams, M., Hook, S., Ramachandran, B., 1999. ASTER user handbook, version 2. Jet Propulsion Laboratory, Pasadena, CA, pp. 1–135.

Albergel, C., Balsamo, G., De Rosnay, P., Muñoz-Sabater, J., Boussetta, S., 2012. A bare ground evaporation revision in the ECMWF land-surface scheme: Evaluation of its impact using ground soil moisture and satellite microwave data. Hydrol. Earth Syst. Sci. 16 (10), 3607–3620. https://doi.org/10.5194/hess-16-3607-2012.

Anderson, M., Kustas, W., 2008. Thermal remote sensing of drought and evapotranspiration. EOS Trans. Am. Geophys. Union. 89 (26), 233–234.

Balsamo, G., Beljaars, A., Scipal, K., Viterbo, P., van den Hurk, B., Hirschi, M., Betts, A.K., 2009. A revised hydrology for the ECMWF model: verification from field site to terrestrial water storage and impact in the integrated forecast system. J. Hydrometeorol. 10 (3), 623–643. https://doi.org/10.1175/2008JHM1068.1.

Berk, A., Anderson, G. P., Acharya, P. K., Bernstein, L. S., Muratov, L., Lee, J., Lewis, P.E., 2005. MODTRAN 5: a reformulated atmospheric band model with auxiliary species and practical multiple scattering options: update. In S. S. Shen & P. E. Lewis (Eds.) (p. 662). https://doi.org/10.1117/12.606026.

Chehbouni, A., Nouvellon, Y., Kerr, Y.H., Moran, M.S., Watts, C., Prevot, L., Goodrich, D. C., Rambal, S., 2001. Directional effect on radiative surface temperature measurements over a semiarid grassland site. Remote Sens. Environ. 76 (3), 360–372.

Chen, Y.-C., Chiu, H.-W., Su, Y.-F., Wu, Y.-C., Cheng, K.-S., 2017. Does urbanization increase diurnal land surface temperature variation? Evidence and implications. Landscape Urban Plann. 157, 247–258.

Cheng, J., Liang, S., Yao, Y., Zhang, X., 2012. Estimating the optimal broadband emissivity spectral range for calculating surface longwave net radiation. IEEE Geosci. Remote Sens. Lett. 10 (2), 401–405.

Marques da Silva, J.R., Damásio, C.V., Sousa, A.M.O., Bugalho, L., Pessanha, L., Quaresma, P., 2015. Agriculture pest and disease risk maps considering MSG satellite data and land surface temperature. Int. J. Appl. Earth Obs. Geoinf. 38, 40–50.

Dash, P., Göttsche, F.-M., Olesen, F.-S., Fischer, H., 2002. Land surface temperature and emissivity estimation from passive sensor data: Theory and practice-current trends. Int. J. Remote Sens. 23 (13), 2563–2594.

Desai, A.R., Khan, A.M., Zheng, T., Paleri, S., Butterworth, B., Lee, T.R., Fisher, J.B., Hulley, G., Kleynhans, T., Gerace, A., Townsend, P.A., Stoy, P., Metzger, S., 2021. Multi-sensor approach for high space and time resolution land surface temperature. Earth Space Sci. 8 (10) https://doi.org/10.1029/2021EA001842.

Donlon, C.J., Minnett, P.J., Jessup, A., Barton, I., Emery, W., Hook, S., Wimmer, W., Nightingale, T.J., Zappa, C., 2014. In: Ship-borne thermal infrared radiometer systems. Academic Press, pp. 305–404.

Duan, S.-B., Li, Z.-L., Leng, P., 2017. A framework for the retrieval of all-weather land surface temperature at a high spatial resolution from polar-orbiting thermal infrared and passive microwave data. Remote Sens. Environ. 195, 107–117.

Duan, S.-B., Li, Z.-L., Li, H., Göttsche, F.-M., Wu, H., Zhao, W., Leng, P., Zhang, X., Coll, C., 2019. Validation of Collection 6 MODIS land surface temperature product using in situ measurements. Remote Sens. Environ. 225, 16–29.

Ermida, S.L., Trigo, I.F., Hulley, G., DaCamara, C.C., 2020. A multi-sensor approach to retrieve emissivity angular dependence over desert regions. Remote Sens. Environ. 237, 111559. https://doi.org/10.1016/j.rse.2019.111559.

Ermida, S.L., Trigo, I.F., DaCamara, C.C., Göttsche, F.M., Olesen, F.S., Hulley, G., 2014. Validation of remotely sensed surface temperature over an oak woodland landscape—the problem of viewing and illumination geometries. Remote Sens. Environ. 148, 16–27.

Fu, P., Xie, Y., Weng, Q., Myint, S., Meacham-Hensold, K., Bernacchi, C., 2019. A physical model-based method for retrieving urban land surface temperatures under cloudy conditions. Remote Sens. Environ. 230, 111191. https://doi.org/10.1016/j.rse.2019.05.010.

GBOV, 2018. Ground-Based Observations for Validation (GBOV) of Copernicus Global Land Products, Algorithm Theoretical Basis Document Land Surface Temperature products, RM2 (Thermal radiation), RM8 (Emissivity) and RM9 (Surface temperature), Ref.: GBOV-ATBD-RM2-RM8-RM9, Version: 1.3.

GCOS, 2016. The global observation system for climate: implementation needs, GCOS-200 (GOOS-214), World Meteorological Organisation, https://library.wmo.int/doc_num.php?explnum_id=3417, accessed 09-07-2020.

Ghilain, N., Arboleda, A., Gellens-Meulenberghs, F., 2011. Evapotranspiration modelling at large scale using near-real time MSG SEVIRI derived data. Hydrol. Earth Syst. Sci. 15 (3), 771–786. https://doi.org/10.5194/hess-15-771-2011.

Gislason, P.O., Benediktsson, J.A., Sveinsson, J.R., 2006. Random forests for land cover classification. Pattern Recogn. Lett. 27 (4), 294–300.

Good, E.J., Ghent, D.J., Bulgin, C.E., Remedios, J.J., 2017. A spatiotemporal analysis of the relationship between near-surface air temperature and satellite land surface temperatures using 17 years of data from the ATSR series. JGR Atmospheres 122 (17), 9185–9210. https://doi.org/10.1002/2017JD026880.

Göttsche, F.M., Olesen, F.S., Trigo, I.F., Bork-Unkelbach, A., Martin, M.A., 2016. Long term validation of land surface temperature retrieved from MSG/SEVIRI with continuous in-situ measurements in Africa. Remote Sens. 8 (5), 410.

Guillevic, P.C., Bork-Unkelbach, A., Gottsche, F.M., Hulley, G., Gastellu-Etchegorry, J.-P., Olesen, F.S., Privette, J.L., 2013. Directional viewing effects on satellite land surface temperature products over sparse vegetation canopies — a multisensor analysis. IEEE Geosci. Remote Sens. 10 (6), 1464–1468.

Guillevic, P.C., Göttsche, F., Nickeson, J., Hulley, G., Ghent, D., Yu, Y., Trigo, I., Hook, S., Sobrino, J.A., Remedios, J., Román, M., Camacho, F., 2018. Land Surface Temperature Product Validation Best Practice Protocol. Version 1.1. In P. Guillevic, F. Göttsche, J. Nickeson & M. Román (Eds.), Best Practice for Satellite-Derived Land Product Validation (p. 58): Land Product Validation Subgroup (WGCV/CEOS), doi: 10.5067/doc/ceoswgcv/lpv/lst.001.

Guillevic, P.C., Privette, J.L., Coudert, B., Palecki, M.A., Demarty, J., Ottlé, C., Augustine, J.A., 2012. Land surface temperature product validation using NOAA's surface climate observation networks-scaling methodology for the visible infrared imager radiometer suite (VIIRS). Remote Sens. Environ. 124, 282–298. https://doi.org/10.1016/j.rse.2012.05.004.

Hook, S.J., Clodius, W.B., Balick, L., Alley, R.E., Abtahi, A., Richards, R.C., Schladow, S. G., 2005. In-flight validation of mid-and thermal infrared data from the Multispectral Thermal Imager (MTI) using an automated high-altitude validation site at Lake Tahoe CA/NV, USA. IEEE Trans. Geosci. Remote Sens. 43 (9), 1991–1999.

Hook, S.J., Vaughan, R.G., Tonooka, H., Schladow, S.G., 2007. Absolute radiometric in-flight validation of mid infrared and thermal infrared data from ASTER and MODIS on the Terra spacecraft using the Lake Tahoe, CA/NV, USA, automated validation site. IEEE Trans. Geosci. Remote Sens. 45 (6), 1798–1807.

Hulley, G.C., Göttsche, F.M., Rivera, G., Hook, S.J., Freepartner, R.J., Martin, M.A., Cawse-Nicholson, K., Johnson, W.R., 2021. Validation and quality assessment of the ECOSTRESS level-2 land surface temperature and emissivity product. IEEE Trans. Geosci. Remote Sens.

Hulley, G.C., Hook, S.J., Hughes, C., 2012. MODIS MOD21 land surface temperature and emissivity algorithm theoretical basis document. Pasadena, CA: Jet Propulsion Laboratory, National Aeronautics and Space Administration, 2012.

Hulley, G.C., Hook, S.J., Baldridge, A.M., 2010. Investigating the effects of soil moisture on thermal infrared land surface temperature and emissivity using satellite retrievals and laboratory measurements. Remote Sens. Environ. 114 (7), 1480–1493.

Jarvis, C.H., Baker, R.H.A., Morgan, D., 2003. The impact of interpolated daily temperature data on landscape-wide predictions of invertebrate pest phenology. Agric. Ecosyst. Environ. 94 (2), 169–181.

Kerr, Y.H., Lagouarde, J.P., Imbernon, J., 1992. Accurate land surface temperature retrieval from AVHRR data with use of an improved split window algorithm. Remote Sens. Environ. 41 (2-3), 197–209.

Kim, J., Hogue, T.S., 2013. Evaluation of a MODIS triangle-based evapotranspiration algorithm for semi-arid regions. J. Appl. Remote Sens. 7 (1), 073493. https://doi.org/10.1117/1.JRS.7.073493.

Langsdale, M.F., Dowling, T.P.F., Wooster, M., Johnson, J., Grosvenor, M.J., de Jong, M. C., Johnson, W.R., Hook, S.J., Rivera, G., 2020. Inter-Comparison of field-and laboratory-derived surface emissivities of natural and manmade materials in support of land surface temperature (LST) remote sensing. Remote Sensing 12 (24), 4127.

Li, M., Zhou, J.i., Peng, Z., Liu, S., Göttsche, F.-M., Zhang, X., Song, L., 2019. Component radiative temperatures over sparsely vegetated surfaces and their potential for upscaling land surface temperature. Agric. For. Meteorol. 276-277, 107600. https://doi.org/10.1016/j.agrformet.2019.05.031.

Li, X., Zhou, Y., Asrar, G.R., Zhu, Z., 2018. Creating a seamless 1 km resolution daily land surface temperature dataset for urban and surrounding areas in the conterminous United States. Remote Sens. Environ. 206, 84–97.

Li, Z.-L., Wu, H., Wang, N., Qiu, S., Sobrino, J.A., Wan, Z., Tang, B.-H., Yan, G., 2013. Land surface emissivity retrieval from satellite data. Int. J. Remote Sens. 34 (9-10), 3084–3127.

Liu, J., Melloh, R.A., Woodcock, C.E., Davis, R.E., Ochs, E.S., 2004. The effect of viewing geometry and topography on viewable gap fractions through forest canopies. Hydrol. Process. 18 (18), 3595–3607.

Liu, Y., Zhang, Y., Huang, K.e., Zu, J., Chen, N., Cong, N., 2020. Increased surface broadband emissivity driven by denser vegetation on the tibetan plateau grassland area. J. Indian Soc. Remote Sens. 48 (12), 1845–1859.

Loveland, T.R., Reed, B.C., Brown, J.F., Ohlen, D.O., Zhu, Z., Yang, L., Merchant, J.W., 2000. Development of a global land cover characteristics database and IGBP DISCover from 1 km AVHRR data. Int. J. Remote Sens. 21 (6-7), 1303–1330.

Martins, J., Trigo, I.F., Ghilain, N., Jimenez, C., Göttsche, F.M., Ermida, S.L., Olesen, F.S., Gellens-Meulenberghs, F., Arboleda, A., 2019. An all-weather land surface temperature product based on MSG/SEVIRI observations. Remote Sensing 11 (24), 3044.

Martins, J.P. & Dutra, E. (2020). Validation Report for All Sky Land Surface Temperature (MLST-AS), SAF/LAND/IM/VR_MLST-AS/1.0, Issue 2, 12/10/2020.

Martins, J.P., Trigo., Freitas, S., Simões, N., 2018. Algorithm Theoretical Basis Document for MSG All-weather Land SAF Surface Temperature (MLSTS), SAF/LAND/IPMA/ATBD_MLSTS/1.0, Issue 2.

McFarland, M.J., Miller, R.L., Neale, C.M., 1990. Land surface temperature derived from the SSM/I passive microwave brightness temperatures. IEEE Trans. Geosci. Remote Sens. 28 (5), 839–845.

Meerdink, S., Roberts, D., Hulley, G., Gader, P., Pisek, J., Adamson, K., King, J., Hook, S. J., 2019a. Plant species' spectral emissivity and temperature using the hyperspectral thermal emission spectrometer (HyTES) sensor. Remote Sens. Environ. 224, 421–435.

Meerdink, S.K., Hook, S.J., Roberts, D.A., Abbott, E.A., 2019b. The ECOSTRESS spectral library version 1.0. Remote Sens. Environ. 230, 111196.
Mira, M., Valor, E., Boluda, R., Caselles, V., Coll, C., 2007. Influence of soil water content on the thermal infrared emissivity of bare soils: Implication for land surface temperature determination. J. Geophys. Res. Earth Surf. 112 (F4).
Ni, W., Li, X., Woodcock, C.E., Caetano, M.R., Strahler, A.H., 1999. An analytical hybrid GORT model for bidirectional reflectance over discontinuous plant canopies. IEEE Transactions on Geoscience and Remote Sensing, 37(Serra, J. (1982). Image analysis and mathematical morphology. London, New York: Academic.2), 987–999.
Orth, R., Dutra, E., Trigo, I.F., Balsamo, G., 2017. Advancing land surface model development with satellite-based Earth observations. Hydrol. Earth Syst. Sci. Copernicus GmbH 21 (5), 2483–2495. https://doi.org/10.5194/hess-21-2483-2017.
Payan, V., Royer, A., 2004. Analysis of temperature emissivity separation (TES) algorithm applicability and sensitivity. Int. J. Remote Sens. 25 (1), 15–37.
Prigent, C., Jimenez, C., Aires, F., 2016. Toward "all weather", long record, and real-time land surface temperature retrievals from microwave satellite observations. J. Geophys. Res.: Atmos. 121 (10), 5699–5717.
Rasmussen, M.O., Gottsche, F.-M., Olesen, F.-S., Sandholt, I., 2011. Directional effects on land surface temperature estimation from Meteosat Second Generation for savanna landscapes. IEEE Trans. Geosci. Remote Sens. 49 (11), 4458–4468.
Reichle, R.H., Kumar, S.V., Mahanama, S.P., Koster, R.D., Liu, Q., 2010. Assimilation of satellite-derived skin temperature observations into land surface models. J. Hydrometeorol. 11 (5), 1103–1122.
Remedios, J., 2012. Sentinel 3 Optical Products and algorithm definition, Land Surface Temperature, accessed: 10/12/2021, document reference number: S3-L2-SD-03-T03-ULNILU-ATBD_L2LST, https://sentinel.esa.int/documents/247904/0/SLSTR_Level-2_LST_ATBD.pdf/8a4322ef-c7e0-4abc-9cac-8f5fd69e1fd7.
Rubio, E., Caselles, V., Coll, C., Valour, E., Sospedra, F., 2003. Thermal–infrared emissivities of natural surfaces: improvements on the experimental set-up and new measurements. Int. J. Remote Sens. 24 (24), 5379–5390.
Schmetz, J., Pili, P., Tjemkes, S., Just, D., Kerkmann, J., Rota, S., Ratier, A., 2002. An introduction to Meteosat second generation (MSG). Bull. Am. Meteorol. Soc. 83 (7), 977–992.
Serra, J., 1982. Image Analysis and Mathematical Morphology. Academic Press, New York.
Sobrino, J.A., Raissouni, N., Li, Z.L., 2001. A comparative study of land surface emissivity retrieval from NOAA data. Remote Sens. Environ. 75 (2), 256–266.
Song, P., Huang, J., Mansaray, L.R., 2019. An improved surface soil moisture downscaling approach over cloudy areas based on geographically weighted regression. Agric. Forest Meteorol. 275, 146–158.
Trigo, I., Boussetta, S., Viterbo, P., Balsamo, G., Beljaars, A., Sandu, I., 2015. Comparison of model land skin temperature with remotely sensed estimates and assessment of surface-atmosphere coupling. J. Geophys. Res.: Atmos. 120 (23), 12096–12111. https://doi.org/10.1002/2015JD023812.
Trigo, I.F., Ermida, S.L., Martins, J.P.A., Gouveia, C.M., Göttsche, F.-M., Freitas, S.C., 2021. Validation and consistency assessment of land surface temperature from geostationary and polar orbit platforms: SEVIRI/MSG and AVHRR/Metop. ISPRS J. Photogram. Remote Sens. 175, 282–297. https://doi.org/10.1016/j.isprsjprs.2021.03.013.
Trigo, I.F., Peres, L.F., DaCamara, C.C., Freitas, S.C., 2008. Thermal land surface emissivity retrieved from SEVIRI/Meteosat. IEEE Trans. Geosci. Remote Sens. 46 (2), 307–315.
van den Hurk, B.J.J.M., Viterbo, P., Beljaars, A.C.M., Betts, A.K., 2000. Offline validation of the ERA40 surface scheme. Technical Memorandum. Technical memorandum ECMWF.
Vancutsem, C., Ceccato, P., Dinku, T., Connor, S.J., 2010. Evaluation of MODIS land surface temperature data to estimate air temperature in different ecosystems over Africa. Remote Sens. Environ. 114 (2), 449–465. https://doi.org/10.1016/j.rse.2009.10.002.
Viterbo, P., Beljaars, A.C.M., 1995. An improved land surface parameterization scheme in the ECMWF model and its validation. J. Clim. 8 (11), 2716–2748. https://doi.org/10.1175/1520-0442(1995)008<2716:AILSPS>2.0.CO;2.
Wan, Z., Dozier, J., 1996. A generalized split-window algorithm for retrieving land surface temperature from space. IEEE Trans. Geosci. Remote Sens., vol. 34, 892–905, 1996.
Wan, Z., 2014. New refinements and validation of the collection-6 MODIS land-surface temperature/emissivity product. Remote Sens. Environ. 140, 36–45.
Zhang, R.-H., Li, Z.-L., Tang, X.-Z., Sun, X.-M., Su, H.-B., Zhu, C., Zhu, Z.-L., 2004. Study of emissivity scaling and relativity of homogeneity of surface temperature. Int. J. Remote Sens. 25 (1), 245–259.